Solar radiation forecasting with deep learning techniques integrating geostationary satellite images

Solar radiation forecasting with deep learning techniques integrating geostationary satellite images

Raimondo Gallo[a,*], Marco Castangia[a,1], Alberto Macii[a], Enrico Macii[c], Edoardo Patti[a,b], Alessandro Aliberti[a]

[a]*Department of Control and Computer Engineering, Politecnico di Torino, 10129 Torino, Italy*
[b]*Energy Center Lab, Politecnico di Torino, 10129 Torino, Italy*
[c]*Interuniversity Department of Regional and Urban Studies and Planning, Politecnico di Torino, 10129 Torino, Italy*

Abstract

The prediction of solar radiation allows estimating photovoltaic systems' power production in advance, guaranteeing a more reliable and stable energy supply. In this work, we present a novel approach for short-term solar radiation forecasting that leverages multi-channel images from the geostationary satellites of the Meteosat series, coupled with GHI values in clear-sky conditions. We propose two distinct deep learning models, a 3D-CNN and a ConvLSTM, to forecast solar radiation in terms of GHI values, up to 6-hours ahead with a temporal granularity of 15 minutes, over a test study area, the city of Turin, Piedmont, Italy. The models have been validated with ground GHI measurements, and the results show that the ConvLSTM consistently outperforms the 3D-CNN for longer forecasting horizons, achieving a MAD of 27.18% and an nRMSE of 0.57 for 6-hours ahead predictions. To motivate the use of satellite images, we compared the performance of our approach with a baseline Smart Persistence model and another benchmark model, which previously achieved state-of-the-art performance on the same data set by exploiting various kinds of meteorological inputs. The proposed models outperform the Smart Persistence for predictions farther than 15-minutes ahead, achieving a Forecast Skill of 0.56 for predictions 6-hours ahead. Furthermore, the comparison shows that using raw satellite images overcomes the performance achievable by solely using meteorological variables, reducing the RMSD by more than 3% and the MAD by 1.37% for prediction horizons greater than 4-hours ahead.

*Corresponding author
Email addresses: raimondo.gallo@polito.it (Raimondo Gallo), marco.castangia@polito.it (Marco Castangia), alberto.macii@polito.it (Alberto Macii), enrico.macii@polito.it (Enrico Macii), edoardo.patti@polito.it (Edoardo Patti), alessandro.aliberti@polito.it (Alessandro Aliberti)
[1]ORCID ID: https://orcid.org/0000-0002-2541-0378

Keywords: Solar radiation forecast, Photovoltaic system, Renewable energy, Satellite, Meteosat, deep learning.
2010 MSC: 00-01, 99-00

Nomenclature

List of Acronyms

$3D-CNN$ 3 Dimensional Convolutional Neural Network

ANN Artificial Neural Network

$ConvLSTM$ Convolutional Long Short-Term Memory

$EUMETSAT$ European Organisation for the Exploitation of Meteorological Satellites

FS Forecast Skill

GHI Global Horizontal Irradiance

IR Infrared

$LSTM$ Long Short-Term Memory

MAD Mean Absolute Deviation

MSG Meteosat Second Generation

$nRMSE$ Normalized Root Mean Square Error

PV Photovoltaic

R^2 Coefficient of Determination

$RMSD$ Root Mean Square Deviation

$RMSE$ Root Mean Square Error

RNN Recurrent Neural Network

$SEVIRI$ Spinning Enhanced Visible and InfraRed Imager

VIS Visible

1. Introduction

As the world population grows, the demand for wealth and electrical energy inevitably increases. Almost 80% of the supplied energy worldwide is produced exploiting fossil fuels, as reported by the International Energy Agency (IEA) relatively to 2020 [1]. The increasing consumption and, jointly, the shortage of these energy sources raises the costs. Therefore, combining these factors with the higher awareness about the impact of nonrenewable fuels on air quality pushes toward adopting of more sustainable and reliable energy sources. Solar photovoltaic (PV) technology is gaining more and more relevance as a counterpart to traditional energy sources. The advantages of using such technology are numerous, and the relatively low cost to deploy the PV panels and their modularity fit well with the idea of a smart grid, a new generation of electricity network which embeds more intelligent devices and strategies for a more efficient supply of electricity. Forecasting of Global Horizontal Irradiance (GHI), defined as the total irradiance received from the Sun measured on a horizontal surface on the Earth and measured in units of $[W/m^2]$, is an essential step in most PV power prediction systems. The dynamics of GHI depend on both deterministic and stochastic factors, and the latter requires the adoption of complex physical and statistical models for efficient forecasting. Therefore, the highly variable nature of solar radiation over time, due to its seasonality and the presence of clouds above, makes the PV technology highly dependent on environmental conditions. The intermittence of the solar power output forces the grid operators to adopt more complex management strategies to preserve the equilibrium between demand and supply. Hence, accurate real-time and future solar radiation forecasting can be extremely useful to ensure efficient exploitation of solar power.

Thanks to deep learning techniques and a large ecosystem of sensors densely disseminated over land or space, such as satellite radiometers, new possibilities are available to improve solar radiation forecasting. A vast collection of satellite data is made accessible to final users through web services, such as the Meteosat and Metop products provided through the EUMETSAT Data Store [2]; obtaining such data opens new scenarios to improve solar radiation forecasting through innovative ideas and strategies. The availability of a wide collection of measurements allows the

exploitation of statistical methods to forecast solar radiation. Such methods are generally suited up to 6-hours ahead, employing sequences of historical data of one or more parameters [3]. Machine learning models, belonging to the non-linear class of statistical models, allow the discovery of relations between inputs and outputs even if the representation is impossible. They can be employed in forecasting problems, such as the forecasting of GHI using as input either time-series of historical solar irradiance data (endogenous inputs) or combining solar irradiance and other variables as exogenous variables (exogenous inputs) [4].

In this work, we propose an innovative methodology for short-term solar radiation forecasts up to 6-hours ahead with a temporal granularity of 15 minutes over a test study area, the city of Turin, Piedmont, Italy, based on deep learning approaches. The multi-channel satellite images, supplied by the 0 Degree service of the MSG geostationary satellites [5], are directly provided as input to the forecasting models together with GHI values in clear-sky conditions. No additional exogenous measurements are employed. The temporal sequences of satellite images are fed independently into two distinct tested deep learning models, a 3D-Convolutional Neural Network (3D-CNN) and a 2D-Convolutional Long-Short-Term Memory (ConvLSTM). The GHI predictions of both models are finally validated using ground GHI measurements collected over the test location by a meteorological station equipped with a pyranometer. The performances of the proposed models are set side by side and compared with a Smart Persistence model to demonstrate the efficiency of the suggested methodology. Finally, the most accurate model for farther horizons is compared with a state-of-the-art benchmark LSTM model, which employs a disparate collection of input exogenous meteorological data.

The remaining sections of this work are organized as follows: Section 2 reviews the most effective machine learning methods in the literature for GHI forecasts employing exogenous data and presents the main contributions of our work. Section 3 gives a thorough description of the employed dataset. Section 4 details the adopted data processing and the main steps of the proposed innovative methodology. Then, Section 5 discusses the prediction results by exploiting different analytical indexes. Finally, Section 6 presents the relevant findings of this work, providing some indications for future works.

2. Related works

The efficiency of machine learning at discovering non-linear relationships between inputs and outputs opens new promising possibilities to improve multi-step ahead solar radiation forecasting [6]. The proposed statistical models can be combined to define hybrid models allowing the merging of different techniques to benefit from the advantages specific to each one [7]. Deep learning is a sub-field of machine learning aiming to discover a deeper understanding of the data by stacking successive layers of representation. Here is an overview of the most relevant studies using deep learning methods, coupled with exogenous features, to forecast solar radiation. At the very core of deep learning, there are the feedforward ANNs, powerful models frequently used to face non-linear regression and classification problems thanks to their efficiency in performing non-linear mapping between input and output variables. ANNs are suited for taking on complex machine learning problems such as weather forecasting, facial recognition, and classification of large datasets of images. Lago et al. [8] designed two ANN models to perform short-term solar radiation forecasting over the Netherlands, up to 6 hours, without needing ground measurements, one for local and the other for global forecasts. The suggested solution achieved more precise results than linear and persistence models. The work offers a valid alternative to local models since no ground measurements are needed, and the irradiance values are extracted from the Meteosat [9] satellite images using different methods, allowing the extension of the analysis to any possible location. The efficiency of ANNs at forecasting is also proved by Wagena et al. [10], who employed an ANN to forecast water streamflows up to 8-days ahead. The ANN model proved significant performance skill outperforming the ARMA counterpart.

Another typology of neural networks in deep learning includes Convolutional Neural Networks (CNNs), which are particularly suited for image and video processing. Jiang et al. [11] proposed a deep network, namely ResnetTL, mainly based on CNN and multi-layer perceptron to extract from MTSAT images cloud spatial patterns and morphology to improve hourly global solar radiation predictions, to be combined with ground target measurements. The deep network is trained over 90 stations in China and validated over five independent stations, and the results yield an R^2 of 0.88 and a minimum RMSE of 84.18 W/m^2. The proposed deep network proves the advantages of integrating spatial patterns extracted from satellite images with deep learning approaches to point information to improve global solar radiation predictions. Guermoui et al. [12] proposed an ensemble approach that combines results from disparate deep learning models, including Gaussian

process regression and CNN, to build a competitive model which improves the performances of multi-step hourly global solar radiation forecasting. They also proved the benefits of including exogenous data, which reduced the nRMSE for all the analyzed forecasting horizons. Pérez et al. [13] worked with a deep learning method to forecast intra-day solar irradiance up to 6-hours ahead. They proposed a 2D-CNN model to detect cloud motion features from past estimated-irradiance images from satellite images. They tested the model for different combinations of inputs and time lags or granularity. Their model outperformed the persistent algorithm in all tests, and Numerical Weather Prediction (NWP) estimates for the same forecasting horizon, proving the benefits of such methodology, especially for very short-term predictions. Choi et al. [14] used a 2D-CNN combined with satellite images to predict solar irradiance over 12 locations in the US for various prediction forecasting horizons, including 30 minutes, 1-hour and 1-day ahead. The infrared 4-channels satellite images are retrieved from NOAA's GOES8 geostationary satellite [15]. Their methodology outperformed persistence models for GHI prediction in all locations for 1-hour ahead predictions, and it highlighted the efficiency of the CNN in handling local and neighboring information to improve long-term forecasting. Yang et al. [16] proposed an approach for short-term GHI forecasting based on exogenous sky images. They used a 3D-CNN model to extract endogenous features from the clear-sky index and exogenous features from sky imagery. The results showed the efficacy of the exogenous features extracted with the deep learning method, proving such methodologies' strength in extracting and integrating new features. Ghimire et al. [17] proposed a hybrid model called CSVR, integrating CNN and Support Vector Regression (SVR) to forecast daily global solar radiation over six solar farms in Queensland, Australia, employing a vast set of exogenous meteorological data. The hybrid CSVR outperformed eight rival benchmark models in terms of R^2, RMSE, and Mean Absolute Error (MAE) over all six sites, exploiting the capabilities of CNN at extracting spatial features and the high prediction accuracy of the SVR.

Finally, Recurrent Neural Networks (RNNs) are widely used to analyze sequential time series data to predict the future. In particular, the Long-Short Term Memory (LSTM) model proved to be very efficient in detecting long-term dependencies in the data; the Gated Recurrent Unit (GRU) model, which is a simplified version of the LSTM, performs just as well [18]. In our previous work [4], we proposed several ML models for GHI short-term forecasting up to 6-hours ahead, including an LSTM model and a 1D-CNN model. The dataset we used is composed of GHI measurements and exogenous features, selected through an accurate feature selection process. The improvement of

the performances for predictions horizons greater than 15 minutes proved the effectiveness of using exogenous inputs, and the LSTM generally performed better than the other suggested models, outperforming the benchmark models. Pang et al. [19] defined an RNN model to prove the contribution of deep learning algorithms for solar radiation forecasting. They aggregated the exogenous data selected to train the model specifying different sampling frequencies, namely 10, 30, and 60 minutes, to investigate their influences on the results. The results proved the RNN to be more accurate than an ANN model trained with the same data, and it also provided smoother results with fewer variations. Furthermore, they verified that higher data frequencies improved the prediction accuracy of the RNN model achieving an RMSE reduction of 16.6% using 10 minutes data instead of 60 minutes data. Benamrou et al. [20] proposed an LSTM-based model for 1-hour ahead GHI forecasting for Al-Hoceima city, Morocco. They used endogenous GHI ground measurements and exogenous satellite-derived GHI. They generated spatio-temporal grids of pixels around the point of interest, from which they extracted the important features, and they tested various scenarios by changing the training data provided to the forecasting model. The results outperformed benchmark approaches and showed the effectiveness of using exogenous features combined with deep learning methods. Ashfaq et al. [21] suggested an LSTM model to forecast GHI 1-hour ahead in Islamabad, Pakistan. They used hourly GHI measurements and exogenous features and, through a fine hyperparameter tuning of the LSTM model, they proved the efficiency of such model forecasting 1-hour ahead using multivariate time series solar irradiance data, accompanied by a substantial decrease for the RMSE incorporating exogenous features. Obiora et al. [22] employed an LSTM network trained with exogenous data selecting a time lag of 60 hours, and they trained the selected model with datasets characterized by different temporal extensions. The LSTM model outperformed the SVR forecasting model, and the best LSTM performances were obtained employing the widest dataset. Sorkun et al. [23] proposed an LSTM model to forecast GHI 1-hour ahead using hourly GHI ground measurements and exogenous data, providing the best performances. The results proved that the LSTM model is suitable for solar forecasting and highlighted the strong dependency of the selected exogenous features on solar radiation. Wojtkiewicz et al. [24] proposed a 1-hour ahead forecasting solution employing a multivariate GRU and LSTM. They evaluated the models using one year of historical solar irradiance data in addition to exogenous weather variables and cloud cover data. The LSTM outperformed the GRU model, and the proposed multivariate models outperformed the univariate models, proving the benefits of including exogenous features and the efficiency of

deep learning models as a counterpart to other ML statistical models. Yu et al. [25] proposed an LSTM model for short-term GHI forecasting for 1-hour and 1-day ahead, including a broad set of exogenous meteorological data, focused on improving the prediction accuracy for cloudy days. Based on the daily GHI and clearness-index, they classified the forecast results as sunny, cloudy, and partially cloudy using the K-means algorithm. The LSTM model outperformed other deep learning and ML models, such as RNN, CNN, ARIMA, and SVR [25], proving the forecasting efficiency of LSTM, especially for cloudy and partially cloudy days. Nielsen et al. [26] presented an approach using convLSTM and 3D-CNN to forecast short-term solar irradiance utilizing ground GHI measurements coupled with exogenous features outperforming the benchmark models for forecasting horizons up to 4-hours ahead, proving the efficiency of satellite-based solar irradiance methods using deep learning. Xiao et al. [27] proved the efficiency of the ConvLSTM at forecasting the sea surface temperature. They employed time series of sea surface temperature grids obtained from satellite data to improve predictions up to 10-days ahead. The proposed ConvLSTM outperformed the Persistent Model, SVR, and LSTM [27] for all the prediction horizons, proving its capabilities at jointly exploiting both temporal and spatial information. Yeom et al. [28] developed a new convLSTM model to forecast solar radiation 1-hour ahead, creating solar radiation maps of the Korean Peninsula using geostationary satellite images. The model showed higher accuracy in predicting solar radiation maps than ANN and Random Forest (RF) reference models. Prado-Rujas et al. [29] proposed a ConvLSTM model to forecast solar radiation up to 1-hour ahead using stacked solar maps generated by interpolating endogenous ground measurements collected from 17 stations on the Island of Oahu, Hawaii. They tested different lag extensions and image sizes of the irradiance maps, and the results were compared with baseline persistence and other deep learning models. The ConvLSTM model provided competing performances achieving a median forecast skill of 21.2% for predictions 61-minutes ahead, outperforming the rival RNN model. Zang et al. [30] defined a hybrid CNN-LSTM model to forecast GHI 1-hour ahead. The hybrid model uses the spatio-temporal correlations to predict GHI 1-hour ahead, over five target sites in Texas, USA, specifying a time lag ranging from 1 to 10 hours. The performances of their suggested methodology are compared with the other eight benchmark models, and the hybrid model achieves the most accurate annual GHI predictions. Furthermore, the hybrid model provided the best forecasting performance for each season of the year, outperforming the rival models for autumn and winter GHI distribution curves.

Our study employs deep learning models coupled with multispectral satellite images. In the

literature, a general approach to forecasting solar radiation, as opposed to our methodology, is employing of time series of meteorological data and exploiting machine learning approaches [3]. In this framework, LSTM and 1D-CNN models proved to be very efficient at forecasting solar radiation up to a few hours ahead, given input sequences of meteorological measurements, outperforming rival models such as Random Forest and Feedforward Neural Networks [4]. Such models have the advantages of dealing with a relatively small number of hyperparameters, reducing the possibility of overfitting and allowing the training and validation phases to be quite fast. Furthermore, time series of input data occupy relatively small disk space, allowing to deal with many input samples. As cons, the employment of time series of meteorological data provided as input to machine learning models requires the deployment of ground sensors in order to collect measurements. Moreover, due to the low data dimensionality of the inputs, the machine learning model might not grasp some interesting characteristics from the input 1D sequences, with the possible worsening of forecasting accuracy for farther horizons. Therefore, our proposed models employ higher dimensional data, requiring deep learning approaches, to improve forecasting performances. Deep learning models using convolutional operations to analyze remote sensing data are gaining more relevance, providing state-of-art results [31, 32]. The analysis of time series images requires deep learning models to extract spatio-temporal information from the inputs. Valuable deep learning models able to extract spatial information over an additional third dimension (e.g. time) are 3D-CNN and ConvLSTM [33]. Indeed, 3D-CNNs can perform convolution spatio-temporally, extending the convolutional capabilities of 2D-CNN that are spatially limited [34]. This way, it is possible to preserve temporal information of the input signal that would be totally collapsed using a 2D convolution [34]. On the other hand, the ConvLSTM is obtained by substituting matrix multiplications at each gate of the LSTM with convolutional operations [35]. Thus, the ConvLSTM combines the convolutional structure of CNN for feature extraction with the capability of the LSTM to extract temporal correlations, ensuring an efficient capture of spatio-temporal correlations from the inputs [35]. In this section, we presented several studies employing such models, demonstrating their efficiency in forecasting different measures, including solar radiation. For these reasons, we chose the 3D-CNN and ConvLSTM models to conduct our analysis. In this work, we present an innovative methodology to forecast short-term GHI, up to 6-hours ahead, over a test study area, the city of Turin, Piedmont, Italy. The inputs to our models are multispectral satellite images and GHI values computed in clear-sky conditions to establish a relationship between satellite images, target GHI, and the alternation of night and

day, respectively. The prediction results are then validated using GHI measurements, sampled by a weather station located in the target area, and equipped with a pyranometer. With respect to the literature solutions, the satellite images are provided as direct input to the proposed forecasting models. Hence, no auxiliary methodology is needed to extract input features from the satellite images. Finally, the proposed models employ raw multispectral satellite images as exclusive exogenous input rather than a vast collection of disparate weather data, as presented in the related works [4]. In this way, the necessity of gathering much heterogeneous sensor data is avoided. The presented work compares the two proposed models, thus giving significant insights into their relative prediction performance. Furthermore, their forecasting performances are compared with the ones of a baseline reference Smart Persistence model. Finally, the models are individually compared with a benchmark LSTM model in literature [4], trained using meteorological data, to evaluate the effectiveness of using raw satellite images as only exogenous inputs for short-term solar radiation forecasting.

3. Dataset description

The employed dataset for solar radiation forecasting comprises GHI measurements, GHI values in clear-sky and multi-channel satellite images provided by the Meteosat family of geostationary satellites managed by EUMETSAT [5]. The whole dataset spans over 6 years, from the 1st of January 2010 to the 31st of December 2015, and it is characterized by a temporal resolution of 15 minutes. Moreover, the GHI data and the satellite images have been synchronized and aligned throughout the whole dataset to ensure correspondence and consistency between the heterogeneous data. The test study area is Turin, a northwest Italian city surrounded by the Alps and characterized by an altitude of 239 meters above sea level. Figure 2a shows the location of Turin within the Italian country, while Figure 2b depicts the study area and surroundings which roughly includes the content of the input satellite images to the proposed methodology. The whole dataset has been split, on a temporal basis, into training, validation, and test sets. The *training set* spans from January 1st, 2010, to June 30th, 2014; the *validation set* spans from July 1st, 2014, to December 31st, 2014; the *test set* includes the whole 2015 year. With this temporal subdivision, the resulting training, validation, and test sets include roughly 75%, 8%, and 17% of the total samples, respectively. The following subsections provide a detailed description of GHI data and satellite images.

3.1. The SEVIRI images

The satellite images are disseminated by the Spinning Enhanced Visible and InfraRed Imager (SEVIRI) instrument aboard the prime Meteosat Second Generation (MSG) satellite, located at 0° longitude [9]. The full-disk Earth images are collected at 12 spectral wavelength channels (8 of which belong to the thermal infrared, 3 to the visible channels, and 1 to the near-infrared channel, as reported in Table 1) with a repeat cycle of 15 minutes, which allows the observation of rapidly changing phenomena on Earth's surface and the up-welling atmosphere [36].

Table 1: An overview of the 12 SEVIRI channels including their identifiers and their central, minimum and maximum wavelengths.

Channel identifiers		Characteristics of spectral band (μm)		
No.	Name	λ_{cen}	λ_{min}	λ_{max}
1	VIS0.6	0.635	0.56	0.71
2	VIS0.8	0.81	0.74	0.88
3	NIR1.6	1.64	1.50	1.78
4	IR3.9	3.90	3.48	4.36
5	WV6.2	6.25	5.35	7.15
6	WV7.3	7.35	6.85	7.85
7	IR8.7	8.70	8.30	9.10
8	IR9.7	9.66	9.38	9.94
9	IR10.8	10.80	9.80	11.80
10	IR12.0	12.00	11.00	13.00
11	IR13.4	13.40	12.40	14.40
12	HRV	Broadband (about 0.40 - 1.10)		

The full-disk images relative to channels 1-11 are characterized by size of 3172x3172 pixels and a spatial resolution of 3 km per pixel. Instead, for channel 12 (HRV), the full-disk image has a size of 11136x5568 pixels, characterized by a higher spatial resolution of 1 km per pixel. Consequently, for the sake of this study, the HRV channel is not used to avoid disrupting the consistency with the other channel satellite images. Therefore, only channels 1-11 are employed. The satellite images are made available through the EUMETSAT Data Store, which provides, for every 15 minutes, the level 1.5 images in the native format (.nat). The product includes the full-disk images for all 11 channels for each timestamp. EUMETSAT provides Python APIs that allow users to interact with the Data Tailor [37], a web service interfacing the Data Store, which allows the customization of the products of interest through a set of operations, such as reformatting them into standard GIS formats, filtering channels, compressing the data, selecting portions of the images and, finally, downloading them. The 11 channels SEVIRI images, relative to a single dataset timestamp, have been downloaded specifying the Network Common Data Form, version 4 (NetCDF4) format and

narrowing down the observed scene to a region of interest (ROI) and re-projecting them using the geographic projection. The selected ROI is centered over Turin, in Italy, comprising the Piedmont region and surroundings and the resulting multi-channel images have a size of 82x82 pixels. The area in the SEVIRI images is depicted in Figure 1 as the Natural Color RGB composite, which has been generated applying the RGB recipes supplied by EUMETSAT, selecting the warm channels exclusively [38]. The blurriness of Figure 1 is due to the relatively low spatial resolution of the employed satellite images. The resulting 11-channels images, coupled with the GHI values in clear-sky, will be the input to the forecasting models. The final image dataset comprises 210172 NetCDF4 files, each relative to a specific timestamp. The missing 161 NetCDF4 files are not available on the EUMETSAT Data center. Therefore it has not been possible to retrieve them.

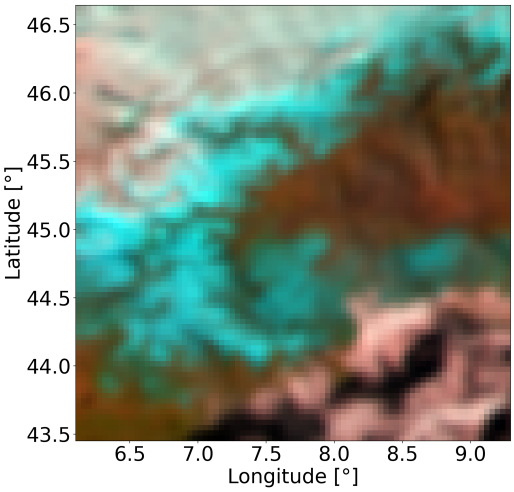

Figure 1: Natural color RGB composite for the selected ROI, 28th of January 2010 at 12:45:00 UTC+0.

3.2. GHI data

The Living Lab, a centralized control unit, has collected solar irradiance data within the Polytechnic of Turin University Campus. The Living Lab collects outdoor data thanks to a meteorological station with sensors measuring temperature, wind speed, atmospheric pressure, precipitation, relative humidity, and solar radiation. However, only the pyranometer solar radiation measurements, expressed in terms of GHI, have been considered. The GHI observations were made available

(a) The location of Turin within the Piedmont region, Italy.

(b) Geographical characteristics of the study area and surroundings.

Figure 2: The location of Turin, the study area of our analysis, depicted as the red dot in the maps.

with a sampling frequency of 15 minutes. Together with the GHI measurements, the clear-sky GHI values have been computed using the Ineichen and Perez model [39] with a sampling frequency of 15 minutes over the same area. Due to either missing or erroneous GHI measurements captured by the pyranometer, we adopted solutions to fix such irregularities, which are deeply discussed in Section 4.3.

4. Methodologies

The standard procedure to forecast GHI consists into specifying a time lag, a series of past observations used to train the forecasting model, and a forecast horizon, the desired predictions ahead in time [40]. Such a framework can be defined as sequence-to-sequence modeling. The learning model receives a multidimensional input sequence with a fixed length. The goal of the model is to predict the output sequence, also characterized by a fixed length, through the discovery of a hypothesis that maps past input values to sequences of future values minimizing a generalization error [41]. In this work, the lag of past observations, i.e., the input sequence, includes multi-channel satellite images, and the forecasting is in the short-term with a horizon up to 6-hours ahead with a step of 15 minutes. Furthermore, to help the model understand the change in daytime and nighttime and the relationship between satellite images and GHI, we supplied an array of GHI clear-sky values, specific to the prediction horizons. To perform GHI forecasting, we tested two distinct models, differing from how the spatio-temporal information is extracted from the lag of satellite images, specifically, the 3D-CNN model and the ConvLSTM model.

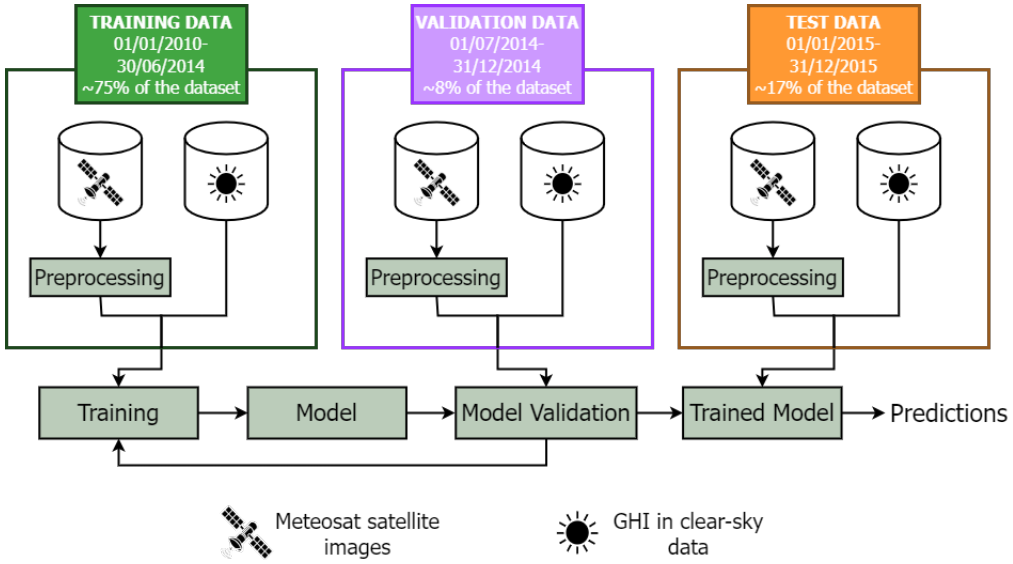

Figure 3: Pipeline with the main steps of the proposed methodology.

Figure 3 shows the main phases of the proposed methodology. Firstly, the training satellite images are preprocessed, as discussed in Section 4.1. Then, once the training data are prepared, the deep learning models are trained to predict GHI values using the selected input data. The same preprocessing used during the training phase is applied to the test set during the test phase. Finally, the forecasting capabilities of the trained models are quantified and compared based on their prediction performances on test data.

4.1. Preprocessing of satellite images

The SEVIRI images, for a given timestamp and each of the 11 spectral wavelength channels, include for each pixel the measured and calibrated effective radiance exiting Earth's atmosphere captured by the SEVIRI instrument. The radiance comes mainly from the Earth's reflection of the Sun's irradiance, and it is measured in $mWm^{-2}sr^{-1}(cm^{-1})^{-1}$. The radiance corresponds to the radiant flux leaving a given surface per unit projected area per unit solid angle. The SEVIRI detectors measure the radiances leaving the extended areas at different wavelengths, and the calibrated radiances are reported within the pixels of each channel image. For a better interpretation of the images, the pixel radiances can be converted to bidirectional reflectance [%], for the solar channels, or brightness temperature [K], for the infrared (IR) channels. In the following sections, we present a detailed description of the conversions and account for the presence of negative radiances during

nighttime and the adopted solution. Finally, to convert the pixel radiances to either reflectance or brightness temperature, the input satellite images are extracted from the NetCDF4 files, and we treat them as a multidimensional array using the Python library *NumPy* [42]. Such a library performs vectorized operations that rapidly execute mathematical operations over a sequence of data. This way, it is possible to manipulate the input channel images efficiently, either converting pixel radiances or normalizing the channel images, as discussed in Section 4.2.

The reflectance of a surface is the efficiency in reflecting radiant energy received by the surrounding environment. Therefore it corresponds to the fraction of electromagnetic radiation that is reflected by a surface. The reflectance is a function of the wavelength of the light, and it can be represented as the ratio between the light leaving a surface and the light hitting the same surface. Thus, reflectance has no unit and can be quantified as a percentage.

The radiances included in the solar SEVIRI channels, VIS0.6, VIS0.8, and NIR1.6, as reported in Table 1, can be converted to reflectance in order to extract information related to clouds and surface during daytime, such as cloud types or whether the surface includes vegetation or not [43]. During the nighttime, the reflectance of the images is equal to zero because, at these frequencies, the dominant radiation source, the Sun, is absent [44]. It is possible to convert radiance to reflectance using the following formula extracted from EUMETSAT documentation [45],

$$r_{\lambda_i} = 100 \cdot \frac{\pi \cdot R_{\lambda_i} \cdot d^2(t)}{I_{\lambda_i} \cdot \cos(\theta(t,x))} \tag{1}$$

where, i is the warm channel number (1 = VIS0.6, 2 = VIS0.8, 3 = NIR1.6), r_{λ_i} is the reflectance for channel λ_i in %, R_{λ_i} is the measured and calibrated radiance in $mWm^{-2}sr^{-1}(cm^{-1})^{-1}$, $d(t)$ is the Sun-Earth distance in astronomical units (AU) at time t, I_{λ_i} is the band solar irradiance for the channel R_{λ_i} at 1 AU in $mWm^{-2}sr^{-1}(cm^{-1})^{-1}$, $\cos(\theta(t,x))$ is the solar zenith angle at time t and location x.

The values of irradiances I_{λ_i} for the different Meteosat Second Generation (MSG) satellites are provided from a lookup table (LUT) in the EUMETSAT documentation, and they are computed by the SEVIRI Solar Channel Calibration system (SSCC) through a vicarious calibration of SEVIRI reflective bands [45], which is a calibration for the warm channels that requires data from outside the MSG system [46]. The band solar irradiances are reported in Table 2 and are particular to the different MSG satellites that collected the images employed in this work. With the aid of the

Python libraries *pvlib* [47] and *pysolar* [48] it has been possible to compute the Earth-Sun distance in AU and the zenith angle by specifying the timestamp of the images and the coordinates of the pixels, specific to the specified region of interest (ROI), extracted from the NetCDF4 file.

The zenith angle was forced to take 80° as the maximum value during the sunset and nighttime to avoid issues and artifacts computing the pixel reflectance values. Because zenith angles close to or higher than 90° would have caused the cosine in Equation 1 to take values too close to 0 or even negative values [49], the latter case would have generated negative reflectances, which are physically incorrect. The reflectances take a minimum value of 0% using such a limitation on the zenith angle. The maximum observed reflectance value might exceed 100%. This event is caused by snow-covered pixels, thick cold clouds or nearby thunderstorms that would provide additional illumination [50].

Table 2: Band Solar Irradiance I_{λ_i} at 1 Astronomical Unit (AU) (expressed in $mWm^{-2}sr^{-1}(cm^{-1})^{-1}$ for the different MSG satellites.

Channel ID	MSG1	MSG2	MSG3
VIS 0.6	65.2296	65.2065	65.5148
VIS 0.8	73.0127	73.1869	73.1807
NIR 1.6	62.3715	61.9923	62.0208

The radiance for the cold, or IR, channels can be converted to brightness temperature, expressed in units kelvin [K] to ease the interpretation of the observations. The brightness temperature measures the radiation in terms of the temperature of a hypothetical black-body emitting an identical amount of radiation as observed at the same wavelength, also called the equivalent black-body. The IMage Processing Facility (IMPF), within Meteosat Second Generation Ground Segment (MSG-GS), finds the brightness temperature of an actual observation through an interpolation technique within the pre-calculated LUTs [51]. Using interpolation, the value search within the pre-calculated LUT might be too time-consuming. Hence a simple relation between observed radiance and corresponding brightness temperature has been proposed in [52], and it is indeed the solution employed in this work. The mentioned relation is the following,

$$T_b = \frac{C_2 \cdot v_c}{\alpha \cdot log[\frac{C_1 \cdot {v_c}^3}{\bar{R}} + 1]} - \frac{\beta}{\alpha} \tag{2}$$

with, $C_1 = 2hc^2$ measured in $mWm^2sr^{-1}(cm^{-1})^{-4}$, $C_2 = \frac{hc}{k}$ measured in $K(cm^{-1})^{-1}$, $\bar{R}$ is

the measured and calibrated radiance in $mWm^{-2}sr^{-1}(cm^{-1})^{-1}$ and α, β and v_c are regression coefficients. The constants c, h, and k are the speed of light, Planck, and Boltzmann constants reported in Table 3. The coefficients α, β and v_c are instead found from a non-linear regression of the pre-generated LUT, and their units are respectively cm^{-1} and K, while α is a scalar. The values of α, β, and v_c for the 8 IR channels are reported in Table 4. A more detailed description of the parameters can be found in EUMETSAT documentation [52]. Such parameters are specific to the MSG satellites that disseminated the images employed in this work. Therefore, the proper coefficient must be used in Equation 2, according to the prime satellite disseminating the images.

Table 3: Values for the constants used in Equation 2.

Constant	Value	Units
Speed of light in vacuum	299792458	ms^{-1}
Planck	$6.62606957 \cdot 10^{-34}$	Js
Bolzmann	$1.380648 \cdot 10^{-23}$	JK^{-1}

Table 4: Values for the regression parameters α, β and v_c in Equation 2 for the different MSG satellites.

	MSG1			MSG2			MSG3		
Channel ID	v_c	α	β	v_c	α	β	v_c	α	β
IR 3.9	2567.330	0.9956	3.410	2568.832	0.9954	3.438	2547.771	0.9915	2.9002
WV 6.2	1598.103	0.9962	2.218	1600.548	0.9963	2.185	1595.621	0.9960	2.0337
WV 7.3	1362.081	0.9991	0.478	1360.330	0.9991	0.470	1360.377	0.9991	0.4340
IR 8.7	1149.069	0.9996	0.179	1148.620	0.9996	0.179	1148.130	0.9996	0.1714
IR 9.7	1034.343	0.9999	0.060	1035.289	0.9999	0.056	1034.715	0.9999	0.0527
IR 10.8	930.647	0.9983	0.625	931.700	0.9983	0.640	929.842	0.9983	0.6084
IR 12.0	839.660	0.9988	0.397	836.445	0.9988	0.408	838.659	0.9988	0.3882
IR 13.4	752.387	0.9981	0.578	751.792	0.9981	0.561	750.653	0.9982	0.5390

For wavelengths below or close to 3 μm, the radiance comes mainly from Earth's reflection of the Sun's irradiance. During the nighttime, when the sunlight is absent, the radiances sensed by SEVIRI for the solar channel and channel IR3.9 assume values close to or equal to 0. In this situation, the noise of the detectors on that band can be greater than the observed scene, causing the radiance to assume negative values but still very close to zero [53]. In this work, the negative radiances have been managed by setting them to 10^{-10}, a positive small constant, not equal to zero, to avoid issues applying the formulas for the radiance conversion to reflectance (Equation 1) and brightness temperature (Equation 2).

As previously mentioned, a few satellite images are unavailable from the EUMETSAT Data

Store for several timestamps. The missing images create discontinuity within the series of available satellite images. A sequence of satellite images is given as input to train the proposed forecasting deep learning models, corresponding to past measurements' temporal lag to predict future solar radiation. The presence of missing images makes some image lag sequences discontinuous. A lag sequence is considered continuous if it includes a subsequent temporal series of images without any gap. Therefore, only contiguous lag sequences of satellite images are selected to train and test the forecasting models, while discontinuous lag sequences are discarded. In such a way, the temporal evolution of the observed scene does not include artifacts, ensuring more precise results. The exclusion of lag sequences including one or more gaps, however, reduces the total available samples by 0.1%, but we believe that the achieved benefits are worth the reduction of input samples, although small. After the processing described in Section 4.3, the GHI dataset does not present such an issue. Thus, the generation of continuous lag sequences exclusively concerns the satellite images.

4.2. Satellite images normalization

Once the processed satellite images dataset is generated, the computed pixel values of reflectances for the warm channels, and of brightness temperature, for the cold IR channels are scaled using a min-max normalization, defined by Equation 3, in order to have pixel values within the range $[0, 1]$. The normalization of the multi-channel images is accomplished by discovering the absolute minimum and maximum pixel values, across all images, for each of the 11 channels. The satellite images' normalization is necessary to give the same magnitude to each feature and speed up the training phase of the proposed forecasting models.

$$X_{norm,i} = \frac{X_{input,i} - min_i}{max_i - min_i} \tag{3}$$

In Equation 3, i refers to the channel number, $X_{input,i}$ is the input channel i satellite image, min_i and max_i are the absolute minimum and maximum pixel values for channel i, respectively, and, finally, $X_{norm,i}$ is the normalized channel image. As mentioned in Section 4.1, we process the satellite channel images with the Numpy Python library [42], which allows the application of element-wise scalar operations. This way, the subtraction and division operations are applied to each pixel value of the input satellite image, achieving very efficient and fast normalization. The normalized dataset and the GHI in clear-sky will be the input to the proposed forecasting models.

4.3. GHI data cleaning

As previously mentioned, the GHI measurements presented a few irregularities, such as missing or erroneous data, that would disrupt the continuity and consistency of the GHI time series employed for the training of the forecasting models. The missing data, probably due to a temporary malfunction of the pyranometer, were replaced using a simple linear interpolation. Moreover, comparing the measured GHI values and the clear-sky GHI values computed using the Ineichen and Perez model [39] disclosed the presence of GHI values exceeding the computed GHI values in clear-sky conditions, which presence is probably due to some uncertainty in the measurements of the pyranometer. In order to fix the erroneous data, the clear-sky GHI has been used to threshold GHI measurements since the clear-sky value corresponds to the maximum value the observed GHI can assume. Using this approach, we rounded the exceeding GHI measurements to their corresponding clear-sky values. Therefore, as a result, the final GHI dataset is composed of 210333 rows, one for each 15 minutes step, including for each timestamp the measured GHI and the computed GHI in clear-sky conditions.

4.4. Deep learning models

The selected deep learning models to perform short-term solar radiation are discussed in the following. We selected two deep learning models, namely 3D-Convolutional Neural Network (3D-CNN) and 2D-Convolutional Long Short Term Memory (ConvLSTM). We performed multi-step ahead predictions with a time step of 15-min up to 6-hours ahead, corresponding to 24 outputs. The maximum prediction horizon was chosen arbitrarily, considering that artificial intelligence methods using satellite images are generally suited for time horizons up to 6-hours ahead [54, 3], and the difficulty in predicting many time steps ahead with a good forecasting error. To implement such models, we used the Python *Keras* [55] library, a high-level neural network API running atop TensorFlow [56], an end-to-end open source platform for machine learning. Firstly, we discuss the building blocks of the selected models individually, and finally, we present the overall methodology.

4.4.1. 3D-Convolutional Neural Network

The CNNs proved to be highly efficient in visual processing tasks thanks to their ability to detect complex data patterns and features from input images. Whenever the inputs to the CNN are videos or temporal sequences of images, rather than simple 2D images, the 3D-CNNs allow the

extraction of features from the data in both spatial and temporal dimensions. With 3D-CNN, the kernel can explore the sequence of images over three dimensions, with the third dimension being time. The 3D kernel will convolve into a cube of multiple contiguous frames stacked together. Therefore, the feature maps are connected to multiple contiguous frames in the previous layer [57]. The 3D kernel will be characterized by a set of weights that can extract one type of feature from the 3D stack of frames, and, in order to extract multiple features from the 3D stack of frames, it is possible to specify different sets of weights for the 3D kernel. Its output can be computed through a 3D convolution defined in Equation 4 [57], considering a neuron located in row x, column y, and in feature map j of the convolutional layer i.

$$z_{ij}^{xyz} = f\left(b_{ij} + \sum_{m} \sum_{p=0}^{P_i-1} \sum_{q=0}^{Q_i-1} \sum_{r=0}^{R_i-1} w_{ijm}^{pqr}\, z_{(i-1)m}^{(x+p)(y+q)(z+r)}\right) \tag{4}$$

Where z_{ij}^{xyz} is the value at position (x, y, z) on the j^{th} feature map in the i^{th} layer, f is the selected activation function, b_{ij} is the bias term for the feature map in layer i, m corresponds to the indexes in the set of feature maps in layer $i-1$ connected to the current feature map, R_i being the size of the 3D kernel over the temporal dimension, P_i and Q_i are the height and width of the kernel respectively, w_{ijm}^{pqr} is the value of the kernel at position (p, q) and frame r connected to the m^{th} feature map in the previous layer and, finally, $z_{(i-1)m}^{(x+p)(y+q)(z+r)}$ is the value at position $(x+p)(y+q)(z+r)$ on the m^{th} feature map in the $(i-1)^{th}$ layer.

The first defined forecasting model employs the 3D-CNN, and it includes two distinct input branches, one with a fully connected layer taking as input an array of 24 GHI clear-sky values relative to the forecast horizons up to 6 hours with a step of 15 minutes. The second input branch includes two 3D convolutional layers to analyze the lag of multi-channel satellite images, followed by two fully connected layers. The two branches are then concatenated together, adding the outputs from both branches into a single branch composed of two fully connected layers in series. Finally, the output layer includes 24 neurons for the prediction horizons up to 6 hours with a step of 15 minutes. The structure of the 3D-CNN model, together with its chosen hyperparameters, is depicted in Figure 4.

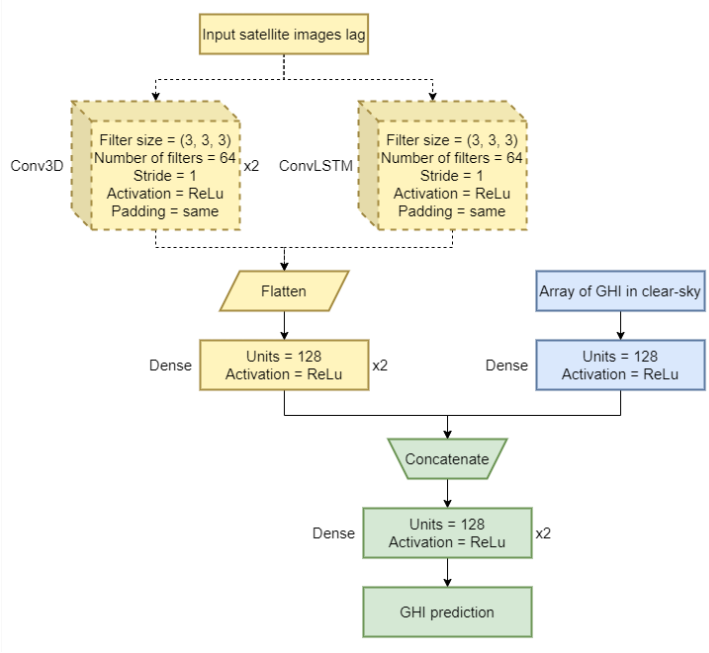

Figure 4: The general structure of the proposed forecasting models and their hyperparameters. The 3D-CNN and ConvLSTM blocks are independently used when defining each of the two analyzed models.

4.4.2. Convolutional-LSTM

Shi proposed a new model [58], the ConvLSTM, which extends convolutional structures to an LSTM to obtain a better capture of spatio-temporal correlations and reduce the accumulated redundancy for spatial data [58]. The proposed model tackles the central issue of LSTM, which is the poor encoding of spatial information due to the employment of fully connected layers within the gate controllers. The proposed model designs the inputs, cell outputs, hidden states, and gates to be 3D tensors, such as images and spatial dimensions. It is also possible to consider as input a 4D tensor with dimensions (sequence, height, width, channels), so a temporal sequence of multi-channel images characterized by a specific size. In such way, the ConvLSTM defines the future state of a cell by the inputs and past states of its local neighbors [58]. The convolution operator is included in the equations performed by the LSTM cell to handle spatial information. Consequently, denoting $\circledast$ as the convolution operator and $\otimes$ as the Hadamard product, the fundamental equations of the ConvLSTM are the following,

$$
\begin{aligned}
\boldsymbol{i}_{(t)} &= \sigma\left(\boldsymbol{W}_{xi} \circledast \boldsymbol{X}_{(t)} + \boldsymbol{W}_{hi} \circledast \boldsymbol{h}_{(t-1)} + \boldsymbol{b}_i\right) \\
\boldsymbol{f}_{(t)} &= \sigma\left(\boldsymbol{W}_{xf} \circledast \boldsymbol{X}_{(t)} + \boldsymbol{W}_{hf} \circledast \boldsymbol{h}_{(t-1)} + \boldsymbol{b}_f\right) \\
\boldsymbol{o}_{(t)} &= \sigma\left(\boldsymbol{W}_{xo} \circledast \boldsymbol{X}_{(t)} + \boldsymbol{W}_{ho} \circledast \boldsymbol{h}_{(t-1)} + \boldsymbol{b}_o\right) \\
\boldsymbol{C}_{(t)} &= \boldsymbol{f}_{(t)} \otimes \boldsymbol{C}_{(t-1)} + \boldsymbol{i}_{(t)} \otimes \tanh\left(\boldsymbol{W}_{xg} \circledast \boldsymbol{X}_{(t)} + \boldsymbol{W}_{hg} \circledast \boldsymbol{h}_{(t-1)} + \boldsymbol{b}_g\right) \\
\boldsymbol{h}_{(t)} &= \boldsymbol{o}_{(t)} \otimes \tanh\left(\boldsymbol{C}_{(t)}\right)
\end{aligned}
\tag{5}
$$

Where, considering time step t, $i_{(t)}, f_{(t)}, o_{(t)}$ are the outputs of input gate, forget gate and output gate, respectively. $X_{(t)}$ is the cell input, $C_{(t)}$ is the cell output and $h_{(t)}$ is the hidden state of a cell. W_{xi}, W_{xf}, W_{xo} and W_{xg} are the weight matrices of the connections to the input X_t, while W_{hi}, W_{hf}, W_{ho} and W_{hg} are the weight matrices of the connections to the previous hidden state $h_{(t-1)}$. The W matrices become now a learnable set of filters. Finally, b_i, b_f, b_o and b_g are the bias terms. A visual representation of the ConvLSTM cell structure is shown in Figure 5.

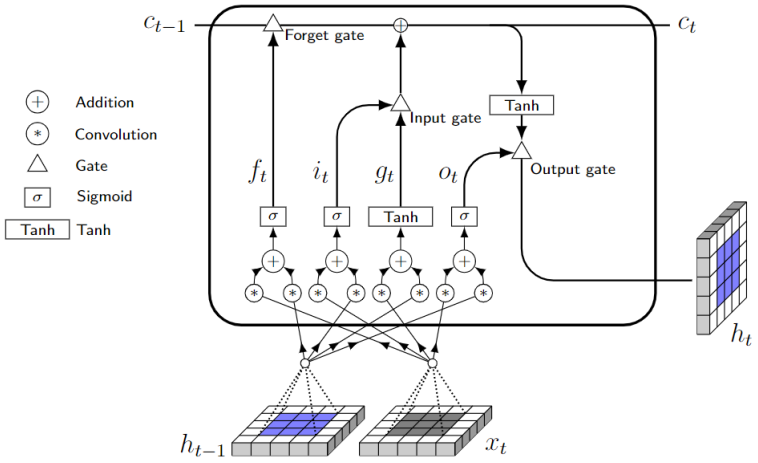

Figure 1: The LSTM cell.

Figure 5: The inner structure of a ConvLSTM.

The second defined forecasting model includes the ConvLSTM, it has the same structure as the models using the 3D-CNN, but it differs from how the spatio-temporal features from the input satellite images are extracted. In particular, the second branch taking the lag of satellite images as input, employs a single ConvLSTM layer, which outputs are passed to a series of two fully connected layers. Besides this variation, the rest of the ConvLSTM model's structure matches the one of the

3D-CNN model. The structure of the ConvLSTM model, together with its chosen hyperparameters, is depicted in Figure 4.

4.5. Configuration and training of the neural network models

For the training hyperparameters of the two models, we chose the Adam optimizer due to its computational efficiency and small memory requirements [59]. We decided to leave the learning rate to its default value after a few trial-and-error tests and observing convergence oscillation due to higher learning rates. We selected the mean squared error as a loss function for our regression task, and we set the number of epochs to 50 to let the model achieve acceptable convergence. Due to the high-memory requirements of the model input and the lag of multi-channel satellite images, we set the batch size to 16 to avoid memory shortage issues. Over-fitting is encountered whenever the error over the testing set gets considerably lower than the one over the validation test. In such a case, the model would become inefficient generalizing the predictions for unseen data. Therefore, to stop the training phase when over-fitting is detected, an early stopping condition is defined, the patience. It specifies the number of epochs with no improvements over the validation set, after which the training phase is interrupted. We set the patience to 3 epochs since over-fitting appeared relatively soon due to a large number of input features. The model with the lowest error over the validation set is selected and tested over the test set. The full description of the adopted training hyperparameters for both proposed forecasting models is reported in Table 5. The training has been conducted employing the following GPU, Nvidia Quadro P1000 with 4GB GDDR5, and a single epoch required approximately 50 to 120 minutes to be completed according to the selected size of the input images.

Table 5: Training hyperparameters.

Hyperparameters	Value
Optimizer	Adam
Loss	Mean squared error
Learning rate	0.001
Epochs	50
Batch size	16
Stopping criteria	Early stopping with patience equal to 3

5. Results and discussion

In the following, we present the prediction results obtained by using the 3D-CNN and the ConvLSTM. Firstly, we present the evaluation metrics used to validate of our models. Then, we briefly discuss the effects of the image size and the lag sequence length on the forecasting performance. After that, we compare the performances of the 3D-CNN and the ConvLSTM for the multi-step ahead forecasting, from 15-min to 6-hours ahead with a temporal granularity of 15 minutes. To conclude, we compare our methodology with a reference Smart Persistence model and the best architecture with a benchmark model that employs meteorological data as exogenous input to demonstrate the advantages of our methodology with respect to the previous methods.

5.1. Performance metrics

In order to evaluate the performance of each method, three standard error metrics are used: the *Root Mean Square Difference* (RMSD), the *Mean Absolute Difference* (MAD), the *Coefficient of determination* (R^2), the *Normalized Root Mean Square Error* (nRMSE), the *Forecast Skill* (FS) and the *Root Mean Square Error* (RMSE); the latter is solely presented since it is used to compute the FS. The RMSD measures the standard deviation of the difference between the observed and predicted values. The MAD measures the absolute difference between observed and predicted values. The R^2 measures the proportion of variability in the observed values that can be explained using the predicted values. The $RMSE$ quantifies the residuals' standard deviation and prediction errors, while the $nRMSE$ is the RMSE normalized by the mean of the observed values. Finally, the FS compares the RMSE values produced by the proposed forecasting models and those from the Smart Persistence model. In this section, it is reported the mathematical formulation of the proposed metrics, where y_{pred} is the predicted values, y_{test} is the observed values, $\overline{y}_{test}$ is the mean value of the observed values, and N is the total number of predictions.

$$RMSD = \frac{100}{\overline{y}_{test}} \sqrt{\frac{\sum_{n=1}^{N} (y_{pred,i} - y_{test,i})^2}{N}} \tag{6}$$

$$MAD = \frac{100}{\overline{y}_{test}} \frac{\sum_{n=1}^{N} |y_{pred,i} - y_{test,i}|}{N} \tag{7}$$

$$R^2 = 1 - \frac{\sum_{n=1}^{N}(y_{test,i} - y_{pred,i})^2}{\sum_{n=1}^{N}(y_{test,i} - \overline{y}_{test})^2} \tag{8}$$

$$RMSE = \sqrt{\frac{\sum_{n=1}^{N}(y_{pred,i} - y_{test,i})^2}{N}} \tag{9}$$

$$nRMSE = \frac{1}{\overline{y}_{test}}\sqrt{\frac{\sum_{n=1}^{N}(y_{pred,i} - y_{test,i})^2}{N}} \tag{10}$$

$$FS = 1 - \frac{RMSE_{forecast}}{RMSE_{SmartPersistence}} \tag{11}$$

5.2. Hyper-parameters optimization

In order to optimize the forecasting performances of the proposed models, we performed a grid search to discover the best configuration of the parameters for the input satellite images. The investigated parameters are the *image size*, 16x16, 32x32, and 64x64 pixels, and the *lag extension*, including 2, 3, and 4 timestamps of 15 minutes. The selection of a unique combination of parameters defines a case study. The two models are independently trained for each case study, and their performances are then compared. Testing all the case studies allowed drawing interesting conclusions about the performances of the two models. For reasons of readability, we report the main achievements in terms of MAD for the most informative case studies in Figure 6. Observing the prediction results, it is generally true that a longer lag allows the achievement of better performances for all proposed metrics, keeping the image size fixed. Indeed, the 3D-CNN trained with images of size 16x16 pixels, obtained for 1-hours ahead predictions a MAD of 21.12, 17.27 and 17.17, selecting a lag of 2, 3, and 4, respectively. Similarly, using 64x64 pixel images to train the ConvLSTM, the MAD for 4-hours ahead forecasts reaches 26.71, 25.9, and 23.97, selecting a lag of 2, 3, and 4, respectively. Figure 6 shows the effect of the lag in terms of MAD for the 3D-CNN and ConvLSTM models, respectively. These results might be pretty intuitive since, as the lag of satellite images extends over a longer time, the models can detect more spatio-temporal information from the observed scene. Consequently, they can grasp the evolution of the dynamics taking place in the scene during the considered lag. Nevertheless, the most interesting result concerns the input

image size. The prediction performances of both models for the different forecasting horizons seem to be directly dependent on the image size. Indeed, with smaller images that include less spatial information, the performance for closer horizons increases, while, on the other hand, employing larger images, the models perform pretty well for farther horizons, worsening the performance for closer horizons. Hence, considering the ConvLSTM and keeping the lag fixed to 4, the RMSD for 30-minutes ahead passes from 35.42% using 16x16 pixel images to 41.28% selecting 64x64 pixel images instead. On the other hand, for 5-hours haead predictions, selecting 16x16 pixel images, the RMSD is 57.13%, whereas using 64x64 pixel images, it reaches 54.3%. It appears to be a direct relationship between data locality and horizon extension, which leads to the intuition that the farther the prediction horizon of interest, the larger should be the spatial extension of the input images. When the target forecast horizon is at most 1 hour, extending the area included in the input images would only worsen the predictions since peripheral data do not bring useful information for the target location. However, as farther horizons are considered, increasing the spatial information of the images allows the models to identify more precisely the dynamics of the observed scene, improving the performances in the long term. The effect of the image size on the performance metrics is shown in Figure 6 in terms of MAD for the 3D-CNN and ConvLSTM, respectively.

The two models provided different performances changing the parameters of the input satellite images. It stands out from the grid search that the 3D-CNN provides better results for closer horizons, up to 1-hour ahead, with smaller images, whereas the ConvLSTM performs better for farther horizons using larger images. As previously stated, longer lags generally ensure both models' more stable and precise results. Therefore, the two optimal case studies to compare the two models are characterized by a lag of 4 and image size of 16x16 pixels for the 3D-CNN, and by a lag of 4 and image size of 64x64 pixels for the ConvLSTM. We compare the performances of the two models, trained by selecting the two optimal case studies, to provide the reader with an overview of their forecasting capabilities, highlighting the strong points of each model. In the following section, a deepened comparison between the two models is carried out in order to highlight their strong points and to select the best-performing model in its entirety.

5.3. Models comparison

Identifying the optimal case studies allows detailed comparison between the two proposed models. We trained the two proposed models selecting the optimal case study that provided the best

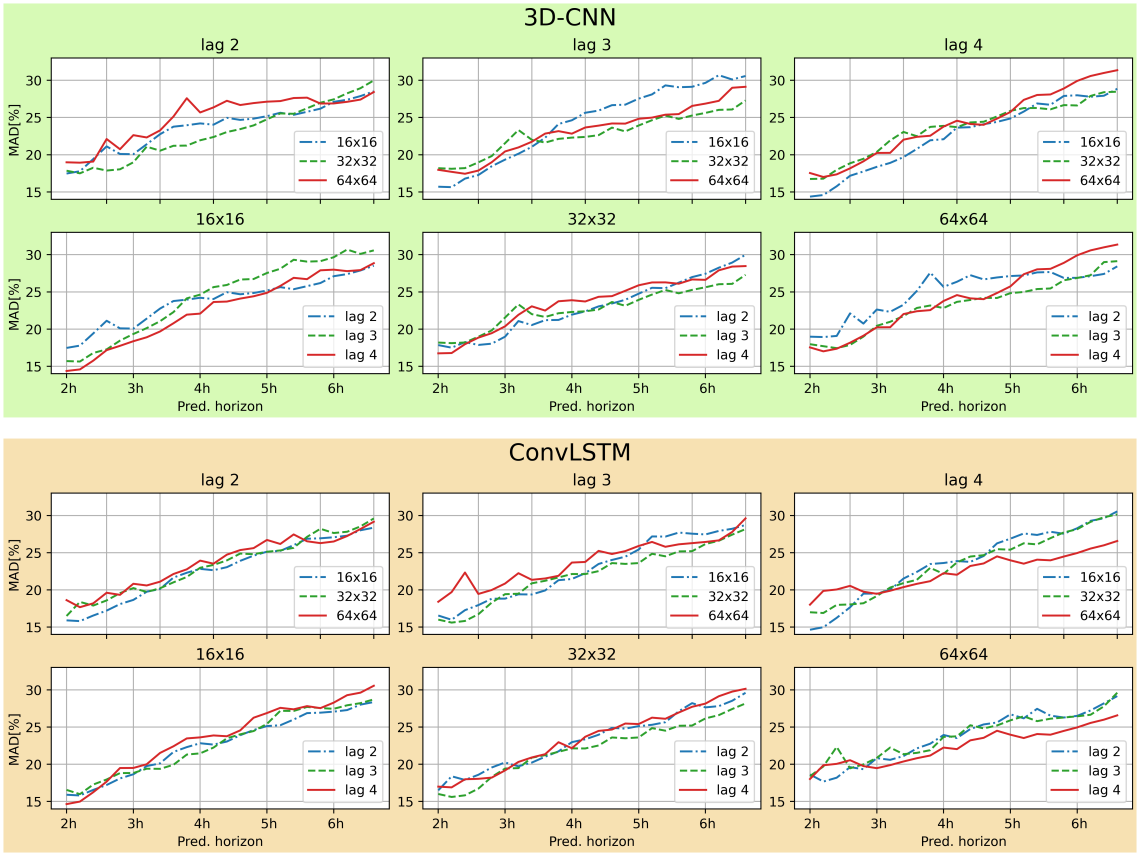

Figure 6: The performances of the 3D-CNN and ConvLSTM models in terms of MAD for all the selected case studies and forecasting horizons.

results, and then analyzed their performances. The forecasting results of both models for 1h, 3h and 6-hours ahead are set against actual observed GHI values for three reference summer winter days belonging to the test set, and they are reported in Figure 7. Both models caught the temporal evolution of the measured GHI, and their prediction results tend to align with the target feature. More precise insight into the achievements of the two models is highlighted by comparing the performance metrics for different horizons, as shown in Figure 8. A full description of the models' results, in terms of MAD, RMSD, R^2, and nRMSE, is reported in Table 6. The ConvLSTM appears more precise than the 3D-CNN for predictions farther than 2 hours. Indeed, observing the models' performances for predictions 3-hours ahead, the ConvLSTM achieves an RMSD of 49.05%, while the 3D-CNN obtains an RMSD of 50.80%. For predictions 6-hours ahead, the RMSD reaches

56.70% for the ConvLSTM and 61.02% for the 3D-CNN. A similar trend is encountered for the MAD, R^2, and nRMSE for horizons farther than 2-hours ahead. The characteristics of the LSTM cell, embedded in the ConvLSTM, allow keeping a memory for both short-term and long-term, which proved such a model to be well suited for more distant temporal predictions.

Considering intra-hour forecasting instead, the 3D-CNN model outperforms the ConvLSTM in terms of all performance metrics. Considering 1-hour ahead predictions, the 3D-CNN achieves a MAD of 17.17%, an nRMSE of 0.40, and an R^2 of 0.94. While the ConvLSTM, for the same forecasting horizon, obtains a MAD of 20.54%, an nRMSE of 0.43 and, finally, an R^2 of 0.93. However, both models experience an accuracy degradation as the prediction horizon moves forward in time due to the accumulation of errors in the forecasting results, making the results from 4-hours ahead quite unreliable. Nonetheless, the accuracy of the multi-step ahead predictions seems relatively stable. The errors increase without unusual behavior as the forecasting horizon increases. In conclusion, the 3D-CNN appears to be more efficient than the ConvLSTM at extracting spatial features from the lag of satellite images, especially when the number of input features is reduced. However, the 3D-CNN is not as performing at exploiting the long-term temporal memory of the observed scene as the ConvLSTM, causing the worsening of the performance for further predictions. Overall, the ConvLSTM outperforms the 3D-CNN for horizons farther than 2 hours in terms of all performance metrics. In order to prove the validity of our methodology, we compare the performances of the proposed models with the ones of a Smart Persistence model and a benchmark LSTM model in literature [4], trained using, as exogenous features, meteorological data exclusively.

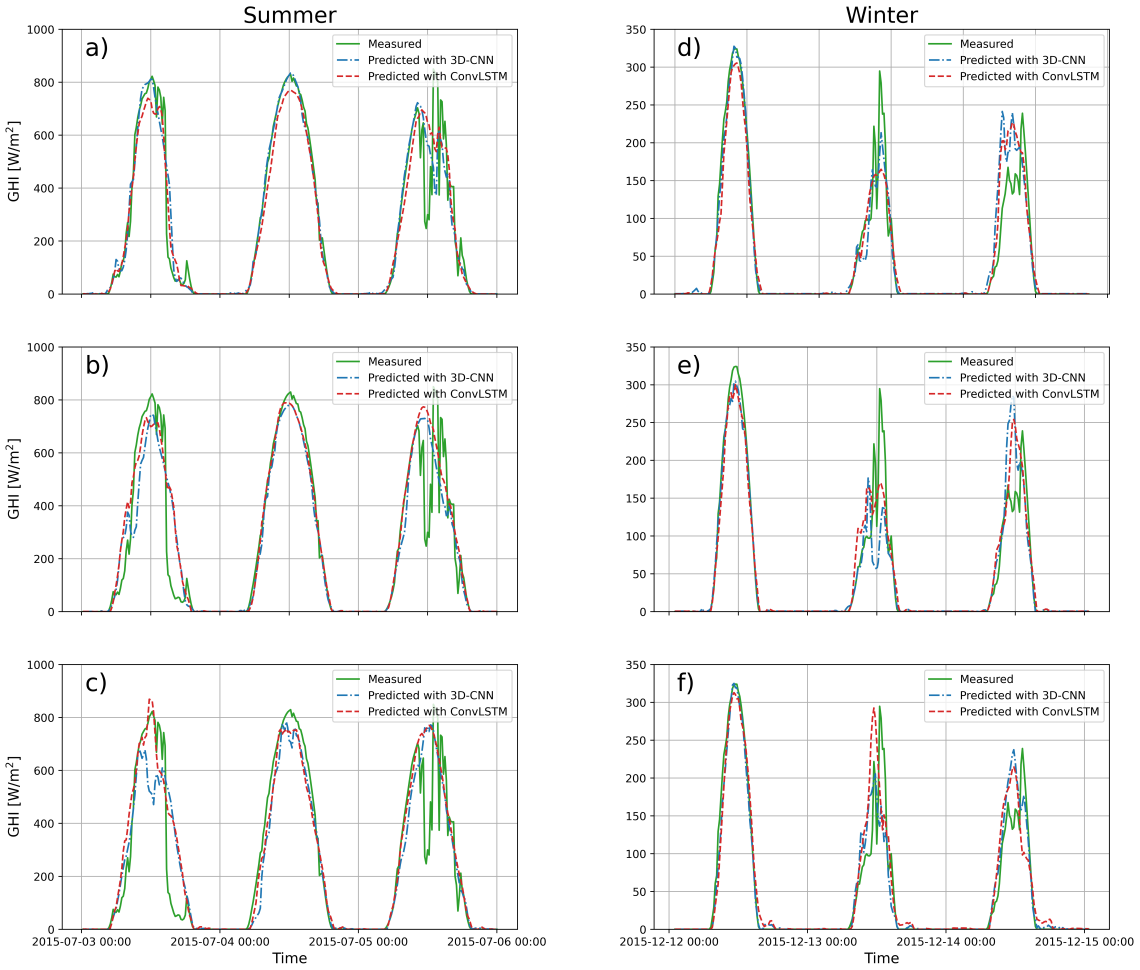

Figure 7: Comparison between seasonal measured and predicted GHI from both models. Figures a), b) and c) show GHI predictions for 1h, 3h and 6h-ahead respectively for three summer reference days. Similarly, figures d), e) and f) show GHI predictions for 1h, 3h and 6h-ahead respectively for three winter reference days.

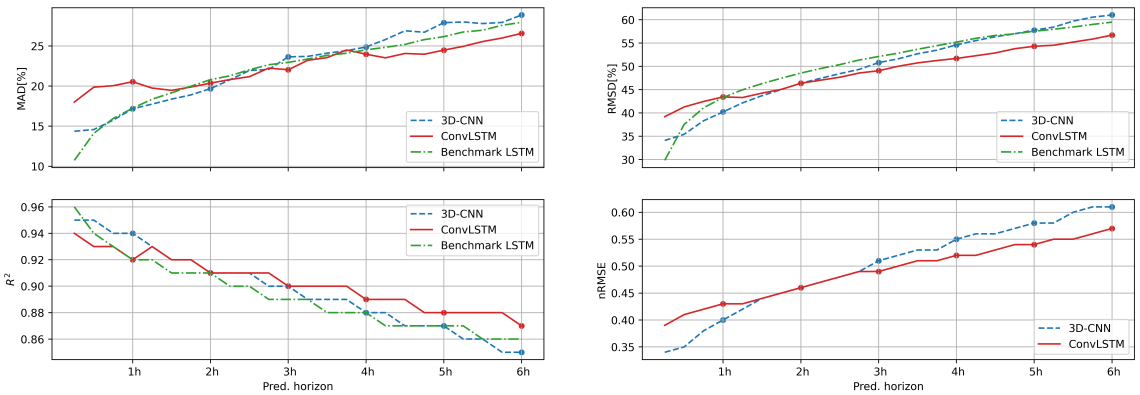

Figure 8: Comparison between 3D-CNN and ConvLSTM in terms of MAD, R^2, RMSD and nRMSE, including also the performances of the benchmark LSTM model using meteorological variables in terms of MAD, R^2 and RMSD.

5.4. Comparison with Smart Persistence model

The Smart Persistence and the Persistence model are the simplest time series model widely used in the solar energy community [60]. The Smart Persistence is a top-performing model for very short-term solar forecasting; hence, it is often used as a baseline to evaluate other forecasting models [60]. The Smart Persistence model is an improvement of the Persistence model since it introduces the clear-sky index correction factor, defined as the ratio between the measured GHI value and GHI computed in clear-sky conditions. The employment of the clear-sky index allows the observation of atmospheric conditions that are then projected into future time. Hence, the forecasts are obtained through the multiplication of the clear-sky index by the future GHI clear-sky. Limitations in modeling atmospheric phenomena generally characterize persistence and Smart Persistence models. Nonetheless they remain efficient intra-hour forecasting models [60]. We implemented a Smart Persistence to quantify the performance improvement of our proposed forecasting models. The selected Smart Persistence is defined in Equation 12 [61],

$$I(t) = \frac{I_0}{I_{clear-sky}(t_0)} \cdot I_{clear-sky}(t) \tag{12}$$

Where I_0 is the 15-minutes time resolution measured GHI at the initial time t_0, $I_{clear-sky}(t_0)$ is the corresponding GHI computed in clear-sky conditions and $I_{clear-sky}(t)$ is the GHI in clear-sky conditions at future time t. The I_0 and $I_{clear-sky}(t_0)$ ratio corresponds to the clear-sky index, which is used to assess solar forecasts. For our use case, the clear-sky index for time t_0 is multiplied by a

vector of clear-sky GHI measurements relative to the future 6 hours with a temporal granularity of 15 minutes, obtaining the GHI forecasts up to 6-hours ahead. We compared the performances of the ConvLSTM and 3D-CNN models with those of the Smart Persistence model to prove the efficiency of the proposed methodology. The Persistence models are generally suited for intra-hour forecasting due to their simplistic approach modeling solar radiation [60]. Indeed, Persistence models do not allow precise solar radiation forecasts for farther horizons. These observations are confirmed by comparing the proposed models' performances with those of the Smart Persistence. The detailed comparison is shown in Figure 9 in terms of all the selected metrics, including the FS, and for all considered forecasting horizons. The Smart Persistence model is very efficient for intra-hour predictions, up to 15-minutes ahead, outperforming our methodology for all the considered metrics. Nonetheless, the proposed models improve the forecasting performances for horizons farther than 15 minutes by a substantial margin. For instance, comparing the prediction results of the ConvLSTM model and those of the Smart Persistence, we obtain an FS of 0.02, 0.36, and 0.56 for horizons of 30-minutes, 3-hours and 6-hours ahead, respectively. Similar FS skills are obtained for the 3D-CNN model. The FS trend and the discussed results confirm the effectiveness of the proposed methodology, proving the efficiency of deep learning models for solar radiation forecasting.

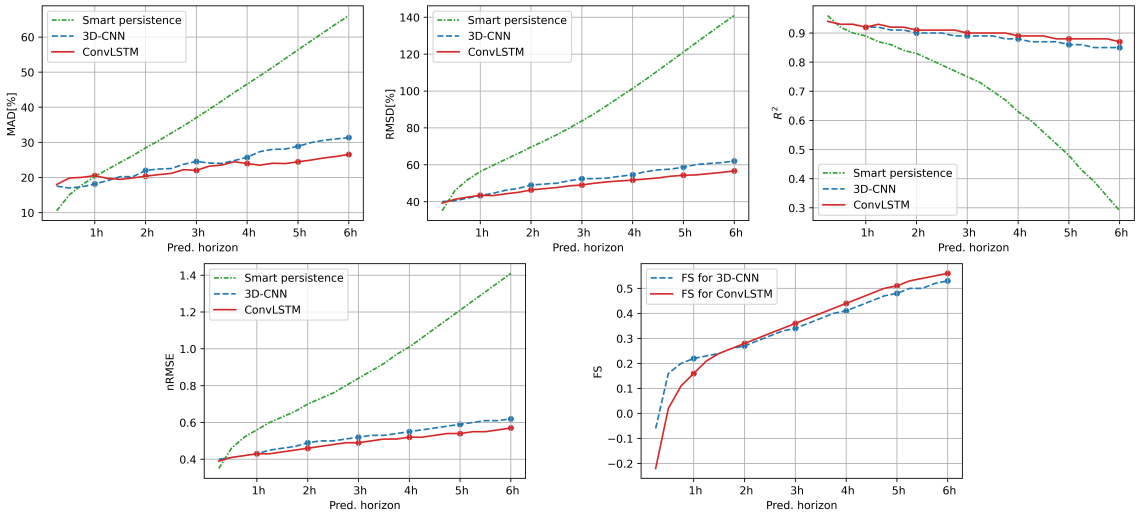

Figure 9: Comparison between 3D-CNN, ConvLSTM and Smart Persistence in terms of all performance metrics together and FS.

5.5. Comparison with benchmark model

The efficiency of satellite images as exclusive input exogenous features is demonstrated by comparing the performances of our proposed models with a benchmark LSTM model in literature [4] trained using exclusively meteorological data as exogenous features. The GHI dataset used to train the LSTM model is the same one we employed for our forecasting models. The same meteorological station has collected it, and it spans over the same period, with a temporal granularity of 15 minutes. Therefore, it is possible to validate the proposed and benchmark models using the same GHI data, which permits a direct performance comparison highlighting the advantages of using exogenous satellite images instead of a vast collection of weather data. Figure 8 shows the performance comparison between our 3D-CNN, ConvLSTM, and the benchmark LSTM models for the common performance metrics and all the investigated prediction horizons. A more detailed comparison of the performances is reported in Table 6. Focusing firstly on closer forecasting horizons up to 2-hours ahead, the LSTM model trained with meteorological data outperformed both proposed models for 15-minutes ahead predictions in terms of all metrics. Nonetheless, the 3D-CNN constantly achieves better forecasting performances from 30-minutes up to 2-hours ahead horizons. Indeed, for 1.5-hours ahead predictions, the 3D-CNN obtains a MAD of 18.37% and a RMSD of 43.69%. In contrast, the rival LSTM model achieves 19.16% and 46.28%, respectively. Observing farther forecasting horizons, ranging from 2 to 6-hours ahead, the ConvLSTM thoroughly outperforms the LSTM model for all the common metrics. As a matter of fact, for 4-hours ahead predictions the proposed ConvLSTM achieves a MAD of 23.97% and an RMSD of 51.69%. While, for the same prediction horizon, the benchmark LSTM model obtains a MAD of 24.51% and an RMSD of 55.19%. The same trend can be observed for 6-hours ahead predictions. The MAD for the ConvLSTM is 26.57%, it reaches 27.94% for the meteorological LSTM, and the RMSD achieves a 2.78% improvement over the benchmark LSTM model. The performance comparison between our satellite-based models and the meteorological LSTM proves our methodology to be very efficient at forecasting solar radiation. The sequence-to-sequence LSTM is outperformed by the 3D-CNN and ConvLSTM, which jointly exploit both temporal and spatial information. Thanks to this property, characterizing the selected deep learning models, our methodology can also utilize peripheral information to the target pixel, which ensures, in both the short and long terms, the improvement of the forecasting results.

Table 6: The results in terms of MAD, RMSD, R^2 and nRMSE for the 3D-CNN and ConvLSTM trained selecting the relative optimal case studies, and in terms of MAD, RMSD, and R^2 for the benchmark LSTM model [4].

Pred. Horizon	3D-CNN				ConvLSTM				Benchmark LSTM [4]		
[hh:mm]	MAD	RMSD	R^2	nRMSE	MAD	RMSD	R^2	nRMSE	MAD	RMSD	R^2
00:15	14.37	34.08	0.95	**0.34**	18.01	39.19	0.94	0.39	**10.74**	**29.81**	**0.96**
00:30	14.58	**34.98**	**0.95**	**0.35**	19.86	41.28	0.93	0.41	**14.11**	37.54	0.94
00:45	**15.76**	**37.32**	**0.94**	**0.38**	20.05	42.45	0.93	0.42	15.96	41.10	0.93
01:00	**17.17**	**39.76**	**0.94**	**0.40**	20.54	43.44	0.92	0.43	17.25	43.31	0.92
01:15	**17.75**	**41.47**	**0.93**	**0.42**	19.75	43.30	0.93	0.43	18.36	44.96	0.92
01:30	**18.37**	**43.69**	**0.92**	**0.44**	19.47	44.24	0.92	0.44	19.16	46.28	0.91
01:45	**18.90**	**45.03**	**0.92**	**0.45**	19.88	45.06	0.92	0.45	19.98	47.45	0.91
02:00	**19.68**	46.37	**0.91**	**0.46**	20.37	**46.36**	0.91	0.46	20.08	48.55	0.91
02:15	**20.78**	47.41	**0.91**	**0.47**	20.81	**47.01**	0.90	0.47	21.28	49.51	0.90
02:30	21.94	48.42	**0.91**	**0.48**	**21.17**	**47.65**	0.90	0.48	22.03	50.36	0.90
02:45	**22.08**	49.34	**0.90**	**0.49**	22.24	**48.56**	0.90	0.49	22.66	51.35	0.89
03:00	23.64	50.80	**0.90**	0.51	**22.03**	**49.05**	0.90	**0.49**	22.95	52.11	0.89
03:15	23.70	51.60	0.89	0.52	**23.21**	**50.01**	**0.90**	**0.50**	23.37	52.82	0.89
03:30	24.10	52.69	0.89	0.53	**23.55**	**50.73**	**0.89**	**0.51**	23.83	53.66	0.88
03:45	**24.41**	53.47	0.89	0.53	24.50	**51.24**	**0.89**	**0.51**	24.09	54.44	0.88
04:00	24.87	54.61	0.88	0.55	**23.97**	**51.69**	**0.89**	**0.52**	24.51	55.19	0.88
04:15	25.80	55.52	0.88	0.56	**23.52**	**52.27**	**0.89**	**0.52**	24.83	56.01	0.87
04:30	26.89	56.35	0.87	0.56	**24.06**	**52.87**	**0.89**	**0.53**	25.19	56.62	0.87
04:45	26.71	56.99	0.87	0.57	**23.97**	**53.78**	**0.88**	**0.54**	25.79	56.98	0.87
05:00	27.90	57.78	0.87	0.58	**24.48**	**54.30**	**0.88**	**0.54**	26.16	57.53	0.87
05:15	27.99	58.41	0.86	0.58	**24.95**	**54.52**	**0.88**	**0.55**	26.74	57.96	0.87
05:30	27.79	59.70	0.86	0.60	**25.55**	**55.20**	**0.88**	**0.55**	26.96	58.44	0.86
05:45	27.93	60.55	0.85	0.61	**25.99**	**55.85**	**0.88**	**0.56**	27.58	58.99	0.86
06:00	28.86	61.02	0.85	0.61	**26.57**	**56.70**	**0.87**	**0.57**	27.94	59.48	0.86

6. Conclusions

In this work, we proposed a new methodology to forecast short-term solar radiation up to 6-hours ahead. The novelty concerns employing the Meteosat multi-channel satellite images as exclusive exogenous data rather than a vast collection of meteorological data. We defined two distinct deep learning models, the 3D-CNN and the ConvLSTM. Overall, the 3D-CNN trained with smaller images achieved better forecasts up to 1-hour ahead, for which the RMSD and MAD reached 39.76% and 17.17%, respectively. On the other hand, the ConvLSTM model provided the best performances for farther horizons using larger images. Indeed, for 6-hours ahead predictions, using the ConvLSTM, the RMSD and MAD reached 56.70% and 26.57%, respectively, against the 61.02% and 28.86% obtained with the 3D-CNN. The ConvLSTM outperformed the 3D-CNN for most of the prediction horizons, thanks to the characteristics of the LSTM cell, which proved to be very efficient at detecting the temporal correlation of the inputs. Nevertheless, both models generally proved such methodology to be particularly effective at detecting the daily GHI trend and improving solar radiation forecasting performances. An interesting consideration, inferred from

the results, is related to the input image size. Indeed, larger input images allow predicting solar radiation for farther horizons with higher accuracy, while, smaller images are more suited for closer prediction horizons. To demonstrate the validity of our methodology, we compared the forecasting results of our satellite-based ConvLSTM to a benchmark LSTM model trained using time series of meteorological data as exogenous features. Our model outperformed the selected state-of-the-art meteorological counterpart for prediction horizons farther than 1 hour, achieving, for 6-hours ahead predictions, an improvement of 1.37%, 2.78%, and 0.01 for the MAD, RMSD, and R^2, respectively. Therefore, we can state that the employment of raw satellite images is a valid alternative to a vast collection of meteorological data, overcoming the necessity to collect and select the most informative features. Consequently, the ubiquitous access to satellite images allows the study area to be extended to any region of interest without including auxiliary exogenous measurements. In order to replicate our methodology, given the data-driven nature of the proposed deep learning models, the equivalent dataset needs to be processed and split into training, validation, and test set, as described in Section 3, and provided as input to the machine learning models designed and developed as reported in Section 4 and Figure 3.

We proposed using raw multi-channel satellite images to forecast solar radiation in this study. However, the use of satellite images poses some limitations to the analysis. Indeed, retrieving such images can be pretty time-consuming since the most straightforward approach to obtaining such images is to interact with the Data Tailor web service, which customizes the requested images to meet the requirements specified by the user. The number of simultaneous customizations is limited due to the finite computational capacity of the servers. Furthermore, the image dataset, spanning from 2010 to 2015, occupies over 60 GB of disk memory, considering the relatively small size of the employed images, 82x82 pixels. Hence, training the proposed models requires a long time, making the grid search to discover the optimal hyperparameters quite time-consuming. Moreover, to carry out the analysis over a specific location, such location must be included in the full-disk Meteosat image. If the area of interest is located far away from the sub-satellite point, the resulting image might be characterized by a low spatial resolution that would worsen the prediction accuracy below expectations. In this case, images collected by other geostationary multispectral satellites closer to the area of interest are a valid alternative to Meteosat images. Finally, for future works we plan to introduce the clear-sky index, which measures the atmosphere clarity, to train the forecasting models and select it as a prediction target since such a choice provides several modeling advantages

together with a higher forecasting accuracy [62]. Moreover, we will consider using 2D decomposition methods, such as the bi-dimensional empirical mode decomposition [63], in order to extract features from the input satellite images which can be employed to enrich the set of inputs. Eventually, new features might be added to the input, such as combinations of channels, or even enriching the analysis including images collected by other satellites, such as Landsat operated by NASA [64] or GOES operated by NOAA [15]

Appendix A. Full characterization of the hyperparameters grid search in terms of MAD, RMSD and R^2.

Table A.7: Grid search results for both models in terms of MAD.

Case study			Forecast horizons [min]																							
Model	**Lag**	**Image size**	15	30	45	60	75	90	105	120	135	150	165	180	195	210	225	240	255	270	285	300	315	330	345	360
3D-CNN	2	16	17.47	17.78	19.42	21.12	20.1	20.07	21.41	22.76	23.77	23.96	24.21	24.04	24.96	24.68	24.85	25.18	25.64	25.36	25.77	26.19	27.11	27.39	27.88	28.52
		32	17.85	17.5	18.25	17.87	18.04	18.98	21.08	20.54	21.2	21.23	21.94	22.38	23.05	**23.44**	23.94	24.76	25.55	25.5	26.24	26.99	27.44	28.25	28.94	29.99
		64	18.98	18.93	19.08	22.11	20.74	22.63	22.32	23.27	25.13	27.59	25.68	26.36	27.25	26.68	26.94	27.13	27.21	27.62	27.67	26.88	26.89	27.11	27.41	28.43
	3	16	15.7	15.64	16.79	17.27	18.45	19.34	20.13	21.06	22.28	24.13	24.63	25.64	25.93	26.66	26.73	27.54	28.11	29.32	29.07	29.13	29.66	30.69	30.11	30.58
		32	18.19	18.11	18.2	18.97	19.82	21.55	23.32	22.01	21.63	22.13	22.3	22.39	22.63	23.64	**23.13**	23.93	24.64	25.26	24.81	25.27	25.62	26.03	26.08	27.29
		64	17.97	17.7	17.44	17.87	18.99	20.44	20.98	21.74	22.84	23.17	22.83	23.66	23.91	24.2	24.18	24.83	24.99	25.38	25.46	26.56	26.87	27.24	29	29.13
	4	16	**14.37**	**14.58**	**15.76**	17.17	**17.75**	**18.37**	**18.9**	19.68	20.78	21.94	22.08	23.64	23.7	24.1	24.41	24.87	25.8	26.89	26.71	27.9	27.99	27.79	27.93	28.86
		32	16.74	16.78	17.97	18.85	19.45	20.37	21.92	23.06	22.49	23.74	23.88	23.71	24.34	24.43	25.15	25.89	26.27	26.28	26.1	26.67	26.62	27.9	28.4	28.47
		64	17.54	17.01	17.36	18.17	19.11	20.24	20.25	22.02	22.4	22.55	23.78	24.57	24.13	24.02	24.85	25.74	27.37	28.03	28.1	28.9	29.92	30.58	30.99	31.36
ConvLSTM	2	16	15.9	15.8	16.55	17.21	18.09	18.65	19.75	20.12	21.65	22.3	22.82	22.64	23.05	23.9	24.6	25.13	25.24	26.01	26.87	26.93	27.07	27.28	28.01	28.36
		32	16.49	18.38	17.89	18.58	19.56	20.24	19.72	20.22	21.01	21.73	22.97	23.35	23.96	24.88	24.79	25.12	25.3	25.65	27.12	28.21	27.64	27.81	28.53	29.6
		64	18.62	17.67	18.19	19.61	19.33	20.82	20.59	21.1	22.13	22.76	23.93	23.52	24.73	25.35	25.61	26.71	26.17	27.45	26.53	26.28	26.5	27.23	28.18	29.16
	3	16	16.55	15.98	17.27	17.95	18.81	18.82	19.4	**19.38**	**19.92**	21.3	**21.46**	22.24	23.48	24.02	24.46	25.42	27.18	27.16	27.7	27.55	27.45	27.92	28.21	28.72
		32	16	15.6	15.82	**16.72**	18.29	19.42	19.48	20.88	21.22	21.67	22.13	22.12	**22.52**	23.6	23.49	**23.6**	24.85	24.51	25.17	25.2	26.16	26.6	27.42	28.17
		64	18.4	19.7	22.33	19.45	19.98	20.85	22.24	21.35	21.53	21.89	23.67	23.75	25.24	24.82	25.21	25.9	26.44	25.79	26.12	26.28	26.44	26.65	27.78	29.61
	4	16	14.64	14.98	16.24	17.66	19.49	19.5	20	21.52	22.41	23.47	23.61	23.87	23.76	24.55	26.25	26.88	27.58	27.38	27.81	27.54	28.28	29.28	29.62	30.55
		32	16.99	16.89	17.98	18.04	18.2	19.17	20.31	20.91	21.35	22.96	22.15	23.69	24.48	24.66	25.47	25.4	26.26	26.11	26.95	27.72	28.15	29.14	29.76	30.14
		64	18.01	19.86	20.05	20.54	19.75	19.47	19.88	20.37	20.81	**21.17**	22.24	**22.03**	23.21	23.55	24.5	23.97	**23.52**	**24.06**	**23.97**	**24.48**	**24.95**	**25.55**	**25.99**	**26.57**

Table A.8: Grid search results for both models in terms of RMSD.

Case study			Forecast horizons [min]																						
Model	**Lag**	**Image size**	15	30	45	60	75	90	105	120	135	150	165	180	195	210	225	240	255	270	285	300	315	330	345	360
3D-CNN	2	16	37.24	38.37	41.6	44.26	43.71	44.07	45.71	47.21	48.4	48.94	49.61	50.15	51.4	51.79	52.49	53.28	54.03	54.68	55.37	56.17	56.89	57.78	58.41	59.44
		32	38.14	38.55	40.35	41.37	42.95	44.47	46.14	47.19	48.36	49.37	50.92	51.57	52.64	53.7	54.59	55.61	56.45	56.38	57.35	57.87	58.21	59	59.81	60.8
		64	40.77	41.19	42.03	45.31	44.75	46.4	46.95	48.05	49.95	53.28	51.55	52.6	53.61	53.59	54.18	54.67	55.18	55.99	56.51	56.72	57.17	58.01	59.15	60.26
	3	16	34.61	35.91	38.78	40.53	42.73	44.37	45.67	47.25	48.59	50.65	51.45	52.96	53.85	55.05	55.48	56.59	57.43	59.23	59.4	59.66	60.54	61.7	61.56	62.15
		32	38.74	39.66	41.05	42.48	43.93	46.03	48.19	48.05	48.52	49.08	49.49	50.07	50.78	51.67	52.39	53.25	54.05	54.78	55.33	56.14	56.61	57.06	58.05	58.34
		64	40.92	40.61	41.33	42.65	44.25	45.88	46.64	47.71	49.39	50.25	50.48	51.88	52.83	53.53	53.63	54.55	54.78	55.83	55.72	56.46	57.15	57.58	58.55	58.89
	4	16	**34.08**	**34.98**	**37.32**	**39.76**	**41.47**	43.69	45.03	46.37	47.41	48.42	49.34	50.8	51.6	52.69	53.47	54.61	55.52	56.35	56.99	57.78	58.41	59.7	60.55	61.02
		32	37.79	39.16	41.7	43.38	44.57	45.93	47.62	48.96	49.12	50.21	50.68	51.06	51.83	52.57	53.55	54.82	55.8	56.42	56.51	57.35	57.66	58.59	59.3	59.7
		64	40.09	40.51	41.92	43.28	44.53	46.18	47.21	49	49.53	50	51.36	52.47	52.51	52.78	53.77	54.57	56.24	57.23	57.64	58.7	60.15	60.7	61.17	62.03
ConvLSTM	2	16	35.61	35.88	37.86	39.76	42.15	**43.17**	**44.69**	46.06	47.42	48.31	**49.05**	49.88	51	51.92	52.78	53.53	54.2	55.07	55.96	56.41	56.93	57.57	58.29	58.87
		32	36.83	38.24	39.28	40.94	42.5	43.84	44.51	**45.61**	**46.71**	**47.4**	48.55	49.39	50.36	51.42	52.03	52.78	53.65	54.43	55.45	56.45	56.68	57.42	58.33	59.39
		64	40.76	40.59	41.26	42.87	43.67	44.75	45.67	46.47	47.24	48.29	49.6	50.02	50.84	51.73	52.44	53.28	53.55	54.74	54.89	55.75	57.13	58.8	59.05	58.39
	3	16	35.78	36.13	38.73	40.48	42.06	43.16	44.58	45.86	47.26	47.78	**48.45**	49.38	50.52	51.54	52.28	53.49	55.32	55.66	56.7	56.91	57.22	57.98	58.66	59.26
		32	37.32	37.54	38.96	40.69	42.68	44.33	45.2	46.58	47.64	48.26	49.24	49.86	50.6	51.44	52.15	53.02	53.38	54.15	54.53	55.48	55.92	56.39	57.12	57.8
		64	40.19	41.75	44.8	43.09	44.35	45.37	47.08	47.09	47.76	48.69	50.06	50.67	52.03	52.16	52.74	53.94	54.62	54.71	55.46	55.91	56.45	56.8	57.7	59.18
	4	16	34.45	35.42	38.31	40.21	42.26	43.27	44.49	46.32	47.49	48.91	49.47	50.28	50.92	52.1	53.52	54.46	55.59	56	56.72	57.13	58	59.11	59.69	60.27
		32	38.48	38.7	40.71	41.58	42.37	43.75	45.28	46.43	47.41	48.89	48.79	50.18	51.29	51.86	53.23	53.73	54.68	55.21	56.11	56.83	57.55	58.35	59.16	59.41
		64	39.19	41.28	42.45	43.44	43.3	44.24	45.06	46.36	47.01	47.65	48.56	**49.05**	**50.01**	**50.73**	**51.24**	**51.69**	**52.27**	**52.87**	**53.78**	**54.3**	**54.52**	**55.2**	**55.85**	**56.7**

Table A.9: Grid search results for both models in terms of R^2.

Case study			Forecast horizons [min]																						
Model	**Lag**	**Image size**	15	30	45	60	75	90	105	120	135	150	165	180	195	210	225	240	255	270	285	300	315	330	345	360
3D-CNN	2	16	0.94	0.94	0.93	0.92	0.92	0.92	0.92	0.91	0.91	0.9	0.9	0.9	0.89	0.89	0.89	0.89	0.88	0.88	0.88	0.87	0.87	0.87	0.86	0.86
		32	0.94	0.94	0.93	0.93	0.93	0.92	0.91	0.91	0.91	0.9	0.9	0.89	0.89	0.88	0.88	0.88	0.87	0.87	0.87	0.87	0.86	0.86	0.86	0.85
		64	0.93	0.93	0.93	0.92	0.92	0.91	0.91	0.91	0.9	0.89	0.89	0.89	0.88	0.89	0.88	0.88	0.88	0.87	0.87	0.87	0.87	0.87	0.86	0.85
	3	16	0.95	0.95	0.94	0.93	0.93	0.92	0.92	0.91	0.91	0.9	0.89	0.89	0.88	0.88	0.88	0.87	0.87	0.86	0.86	0.86	0.85	0.85	0.85	0.85
		32	0.94	0.94	0.93	0.93	0.92	0.92	0.91	0.91	0.91	0.9	0.9	0.9	0.9	0.89	0.89	0.89	0.88	0.88	0.88	0.87	0.87	0.87	0.87	0.86
		64	0.93	0.93	0.93	0.93	0.92	0.92	0.91	0.91	0.9	0.9	0.9	0.89	0.89	0.89	0.88	0.88	0.88	0.88	0.88	0.87	0.87	0.87	0.86	0.86
	4	16	**0.95**	**0.95**	**0.94**	**0.94**	**0.93**	0.92	**0.92**	0.91	**0.91**	0.91	0.9	0.9	0.89	0.89	0.89	0.88	0.88	0.87	0.87	0.87	0.86	0.86	0.85	0.85
		32	0.94	0.94	0.93	0.92	0.92	0.92	0.91	0.9	0.9	0.9	0.9	0.9	0.89	0.89	0.89	0.88	0.88	0.87	0.87	0.87	0.87	0.86	0.86	0.86
		64	0.94	0.93	0.93	0.92	0.92	0.91	0.91	0.9	0.9	0.9	0.89	0.89	0.89	0.89	0.88	0.88	0.87	0.87	0.87	0.86	0.86	0.85	0.85	0.85
ConvLSTM	2	16	0.95	0.95	0.94	0.94	0.93	0.93	0.92	**0.92**	0.91	**0.91**	0.9	0.9	0.9	0.89	0.89	0.89	0.88	0.88	0.87	0.87	0.87	0.87	0.86	0.86
		32	0.95	0.94	0.94	0.93	0.93	0.92	0.92	0.92	0.91	0.91	0.91	0.9	0.9	0.89	0.89	0.89	0.88	0.88	0.88	0.87	0.87	0.87	0.86	0.86
		64	0.93	0.93	0.93	0.93	0.92	0.92	0.92	0.91	0.91	0.91	0.9	0.9	0.9	0.89	0.89	0.89	0.89	0.88	0.88	0.88	0.87	0.86	0.86	0.86
	3	16	0.95	0.95	0.94	0.93	0.93	0.93	0.92	0.92	0.91	0.91	0.91	0.9	0.9	0.89	0.89	0.89	0.88	0.88	0.87	0.87	0.87	0.87	0.86	0.86
		32	0.94	0.94	0.94	0.93	0.93	0.92	0.92	0.91	0.91	0.91	0.9	0.9	0.9	0.89	0.89	0.89	0.89	0.88	0.88	0.88	0.87	0.87	0.87	0.87
		64	0.94	0.93	0.92	0.93	0.92	0.92	0.91	0.91	0.91	0.91	0.9	0.9	0.89	0.89	0.89	0.88	0.88	0.88	0.88	0.87	0.87	0.87	0.87	0.86
	4	16	0.95	0.95	0.94	0.94	0.93	**0.93**	0.92	0.91	0.91	0.9	0.9	0.9	0.9	0.89	0.89	0.88	0.88	0.87	0.87	0.87	0.87	0.86	0.86	0.85
		32	0.94	0.94	0.93	0.93	0.93	0.92	0.92	0.91	0.91	0.9	0.9	0.9	0.89	0.89	0.89	0.88	0.88	0.88	0.87	0.87	0.87	0.86	0.86	0.86
		64	0.94	0.93	0.93	0.92	0.93	0.92	0.92	0.91	0.91	0.91	**0.91**	**0.9**	**0.9**	**0.9**	**0.9**	**0.89**	**0.89**	**0.89**	**0.88**	**0.88**	**0.88**	**0.88**	**0.88**	**0.87**

References

[1] IEA, Key world energy statistics 2021, https://iea.blob.core.windows.net/assets/52f66a88-0b63-4ad2-94a5-29d36e864b82/KeyWorldEnergyStatistics2021.pdf (2021).

[2] EUMETSAT, Eumetsat data store, https://www.eumetsat.int/eumetsat-data-store, Accessed: 2021-12-01.

[3] C. Voyant, G. Notton, S. Kalogirou, M.-L. Nivet, C. Paoli, F. Motte, A. Fouilloy, Machine learning methods for solar radiation forecasting: A review, Renewable Energy 105 (2017) 569–582. doi:https://doi.org/10.1016/j.renene.2016.12.095.
URL https://www.sciencedirect.com/science/article/pii/S0960148116311648

[4] M. Castangia, A. Aliberti, L. Bottaccioli, E. Macii, E. Patti, A compound of feature selection techniques to improve solar radiation forecasting, Expert Systems with Applications 178 (2021) 114979. doi:https://doi.org/10.1016/j.eswa.2021.114979.
URL https://www.sciencedirect.com/science/article/pii/S0957417421004206

[5] EUMETSAT, Msg 0 degree service, https://www.eumetsat.int/0-degree-service, Accessed: 2021-12-01.

[6] M. Guermoui, F. Melgani, C. Danilo, Multi-step ahead forecasting of daily global and direct solar radiation: A review and case study of ghardaia region, Journal of Cleaner Production 201 (2018) 716–734. doi:https://doi.org/10.1016/j.jclepro.2018.08.006.
URL https://www.sciencedirect.com/science/article/pii/S0959652618323370

[7] M. Guermoui, F. Melgani, K. Gairaa, M. L. Mekhalfi, A comprehensive review of hybrid models for solar radiation forecasting, Journal of Cleaner Production 258 (2020) 120357. doi:https://doi.org/10.1016/j.jclepro.2020.120357.
URL https://www.sciencedirect.com/science/article/pii/S0959652620304042

[8] J. Lago, K. De Brabandere, F. De Ridder, B. De Schutter, Short-term forecasting of solar irradiance without local telemetry: A generalized model using satellite data, Solar Energy 173 (2018) 566–577. doi:https://doi.org/10.1016/j.solener.2018.07.050.
URL https://www.sciencedirect.com/science/article/pii/S0038092X18307138

[9] EUMETSAT, Meteosat second generation (msg), https://www.eumetsat.int/meteosat-second-generation, Accessed: 2021-12-01.

[10] M. B. Wagena, D. Goering, A. S. Collick, E. Bock, D. R. Fuka, A. Buda, Z. M. Easton, Comparison of short-term streamflow forecasting using stochastic time series, neural networks, process-based, and bayesian models, Environmental Modelling & Software 126 (2020) 104669. doi:https://doi.org/10.1016/j.envsoft.2020.104669.
URL https://www.sciencedirect.com/science/article/pii/S1364815219308047

[11] H. Jiang, N. Lu, J. Qin, W. Tang, L. Yao, A deep learning algorithm to estimate hourly global solar radiation from geostationary satellite data, Renewable and Sustainable Energy Reviews 114 (2019) 109327. doi:https://doi.org/10.1016/j.rser.2019.109327.
URL https://www.sciencedirect.com/science/article/pii/S1364032119305350

[12] M. Guermoui, S. Benkaciali, K. Gairaa, K. Bouchouicha, T. Boulmaiz, J. Boland, A novel ensemble learning approach for hourly global solar radiation forecasting, Neural Computing and Applications 34 (2022) 1–23. doi:10.1007/s00521-021-06421-9.

[13] E. Pérez, J. Pérez, J. Segarra-Tamarit, H. Beltran, A deep learning model for intra-day forecasting of solar irradiance using satellite-based estimations in the vicinity of a pv power plant, Solar Energy 218 (2021) 652–660. doi:https://doi.org/10.1016/j.solener.2021.02.033.
URL https://www.sciencedirect.com/science/article/pii/S0038092X21001353

[14] M. Choi, B. Rachunok, R. Nateghi, Short-term solar irradiance forecasting using convolutional neural networks and cloud imagery, Environmental Research Letters 16 (4) (2021) 044045. doi:10.1088/1748-9326/abe06d.
URL https://doi.org/10.1088/1748-9326/abe06d

[15] NOAA, Noaa geostationary satellite server, https://www.goes.noaa.gov/index.html, Accessed: 2021-12-01.

[16] H. Yang, L. Wang, C. Huang, X. Luo, 3d-cnn-based sky image feature extraction for short-term global horizontal irradiance forecasting, Water 13 (13). doi:10.3390/w13131773.
URL https://www.mdpi.com/2073-4441/13/13/1773

[17] S. Ghimire, B. Bhandari, D. Casillas-Pérez, R. C. Deo, S. Salcedo-Sanz, Hybrid deep cnn-svr algorithm for solar radiation prediction problems in queensland, australia, Engineering Applications of Artificial Intelligence 112 (2022) 104860. doi:https://doi.org/10.1016/j.engappai.2022.104860.
URL https://www.sciencedirect.com/science/article/pii/S0952197622001099

[18] P. Kumari, D. Toshniwal, Deep learning models for solar irradiance forecasting: A comprehensive review, Journal of Cleaner Production 318 (2021) 128566. doi:https://doi.org/10.1016/j.jclepro.2021.128566.
URL https://www.sciencedirect.com/science/article/pii/S0959652621027736

[19] Z. Pang, F. Niu, Z. O'Neill, Solar radiation prediction using recurrent neural network and artificial neural network: A case study with comparisons, Renewable Energy 156 (2020) 279–289. doi:https://doi.org/10.1016/j.renene.2020.04.042.
URL https://www.sciencedirect.com/science/article/pii/S0960148120305747

[20] B. Benamrou, M. Ouardouz, I. Allaouzi, M. Ahmed, A proposed model to forecast hourly global solar irradiation based on satellite derived data, deep learning and machine learning approaches, Journal of Ecological Engineering 21 (2020) 26–38. doi:10.12911/22998993/119795.
URL https://doi.org/10.12911/22998993/119795

[21] Q. Ashfaq, A. Ulasyar, H. S. Zad, A. Khattak, K. Imran, Hour-ahead global horizontal irradiance forecasting using long short term memory network, in: 2020 IEEE 23rd International Multitopic Conference (INMIC), 2020, pp. 1–6. doi:10.1109/INMIC50486.2020.9318154.

[22] C. N. Obiora, A. Ali, A. N. Hasan, Forecasting hourly solar irradiance using long short-term memory (lstm) network, in: 2020 11th International Renewable Energy Congress (IREC), 2020, pp. 1–6. doi:10.1109/IREC48820.2020.9310449.

[23] M. C. Sorkun, O. D. Incel, C. Paoli, Time series forecasting on multivariate solar radiation data using deep learning (lstm), Turkish Journal of Electrical Engineering and Computer Sciences 28 (2020) 211–223. doi:10.3906/elk-1907-218.
URL https://journals.tubitak.gov.tr/elektrik/vol28/iss1/15

[24] J. Wojtkiewicz, M. Hosseini, R. Gottumukkala, T. Chambers, Hour-ahead solar irradiance forecasting using multivariate gated recurrent units, Energies 12 (2019) 4055. doi:10.3390/en12214055.
URL https://www.mdpi.com/1996-1073/12/21/4055

[25] Y. Yu, J. Cao, J. Zhu, An lstm short-term solar irradiance forecasting under complicated weather conditions, IEEE Access 7 (2019) 145651–145666. doi:10.1109/ACCESS.2019.2946057.

[26] A. H. Nielsen, A. Iosifidis, H. Karstoft, Irradiancenet: Spatiotemporal deep learning model for satellite-derived solar irradiance short-term forecasting, Solar Energy 228 (2021) 659–669. doi:https://doi.org/10.1016/j.solener.2021.09.073.
URL https://www.sciencedirect.com/science/article/pii/S0038092X21008306

[27] C. Xiao, N. Chen, C. Hu, K. Wang, Z. Xu, Y. Cai, L. Xu, Z. Chen, J. Gong, A spatiotemporal deep learning model for sea surface temperature field prediction using time-series satellite data, Environmental Modelling & Software 120 (2019) 104502. doi:https://doi.org/10.1016/j.envsoft.2019.104502.
URL https://www.sciencedirect.com/science/article/pii/S1364815218312295

[28] J.-M. Yeom, R. C. Deo, J. F. Adamowski, S. Park, C.-S. Lee, Spatial mapping of short-term solar radiation prediction incorporating geostationary satellite images coupled with deep convolutional LSTM networks for south korea, Environmental Research Letters 15 (9) (2020) 094025. doi:10.1088/1748-9326/ab9467.
URL https://doi.org/10.1088/1748-9326/ab9467

[29] I.-I. Prado-Rujas, A. García-Dopico, E. Serrano, M. S. Pérez, A flexible and robust deep learning-based system for solar irradiance forecasting, IEEE Access 9 (2021) 12348–12361. doi:10.1109/ACCESS.2021.3051839.

[30] H. Zang, L. Liu, L. Sun, L. Cheng, Z. Wei, G. Sun, Short-term global horizontal irradiance forecasting based on a hybrid cnn-lstm model with spatiotemporal correlations, Renewable Energy 160 (2020) 26–41. doi:https://doi.org/10.1016/j.renene.2020.05.150.
URL https://www.sciencedirect.com/science/article/pii/S0960148120308557

[31] S. Jing, T. Chao, Time series land cover classification based on semi-supervised convolutional long short-term memory neural networks, The International Archives of the Photogrammetry, Remote Sensing and Spatial Information Sciences XLIII-B2-2020 (2020) 1521–1528. doi:10.5194/isprs-archives-XLIII-B2-2020-1521-2020.
URL https://www.int-arch-photogramm-remote-sens-spatial-inf-sci.net/XLIII-B2-2020/1521/2020/

[32] J. Ball, K. Petrova, D. A. Coomes, S. Flaxman, Using deep convolutional neural networks to forecast spatial patterns of amazonian deforestation, bioRxivdoi:10.1101/2021.12.14.472442.
URL https://www.biorxiv.org/content/early/2021/12/15/2021.12.14.472442

[33] B. C. Llinet, A. e Silva Rodrigo, M. C. M. Ángel, C. Calimanut-Ionut, Review on spatio-temporal solar forecasting methods driven by in situ measurements or their combination with satellite and numerical weather prediction (nwp) estimates, Energies 15 (12). doi:10.3390/en15124341.
URL https://www.mdpi.com/1996-1073/15/12/4341

[34] D. Tran, L. Bourdev, R. Fergus, L. Torresani, M. Paluri, Learning spatiotemporal features with 3d convolutional networks, 2015, pp. 4489–4497. doi:10.1109/ICCV.2015.510.

[35] G. K. D. Teyou, Convlstm for spatio-temporal feature extraction in time-series images, in: Tackling Climate Change with Machine Learning workshop at NeurIPS 2020, 2020.

[36] J. Schmetz, P. Pili, S. Tjemkes, D. Just, J. Kerkmann, S. Rota, A. Ratier, An introduction to meteosat second generation (msg), Bulletin of the American Meteorological Society 83 (2002) 977–992. doi:10.1175/1520-0477(2002)083<0977:AITMSG>2.3.CO;2.
URL https://journals.ametsoc.org/view/journals/bams/83/7/1520-0477_2002_083_0977_aitmsg_2_3_co_2.xml

[37] EUMETLab, Eumetlab data services, https://gitlab.eumetsat.int/eumetlab/data-services, Accessed: 2021-12-01.

[38] EUMETRAIN, Compilation of rgb recipes, http://www.eumetrain.org/RGBguide/recipes/RGB_recipes.pdf, Accessed: 2021-12-01.

[39] P. Ineichen, R. Perez, A new airmass independent formulation for the linke turbidity coefficient, Solar Energy 73 (3) (2002) 151–157. doi:https://doi.org/10.1016/S0038-092X(02)00045-2.
URL https://www.sciencedirect.com/science/article/pii/S0038092X02000452

[40] O. Surakhi, M. A. Zaidan, P. L. Fung, N. Hossein Motlagh, S. Serhan, M. AlKhanafseh, R. M. Ghoniem, T. Hussein, Time-lag selection for time-series forecasting using neural network and heuristic algorithm, Electronics 10 (20). doi:10.3390/electronics10202518.
URL https://www.mdpi.com/2079-9292/10/20/2518

[41] V. Kuznetsov, Z. Mariet, Foundations of sequence-to-sequence modeling for time seriesdoi:10.48550/ARXIV.1805.03714.
URL https://arxiv.org/abs/1805.03714

[42] Numpy website, https://numpy.org/doc/stable/index.html, Accessed: 2021-12-01.

[43] E. S. Agency, Meteosat Second Generation The Satellite Development, ESA Publications Division, ESTEC, P.O. Box 299 2200 AG Noordwijk The Netherlands, 1999.

[44] J. Kerkmann, H. J. Lutz, M. König, Msg channels interpretation guide, https://rammb.cira.colostate.edu/wmovl/vrl/pptlectures/eumetsat/PowerPoints/Channels/solarguide.ppt, Accessed: 2021-12-01 (2004).

[45] EUMETSAT, Conversion from radiances to reflectances for seviri warm channels, https://www-cdn.eumetsat.int/files/2020-04/pdf_msg_seviri_rad2refl.pdf, Accessed: 2021-12-01 (2012).

[46] EUMETSAT, Msg calibration, https://www.eumetsat.int/msg-calibration, Accessed: 2021-12-01.

[47] Pysolar website, https://pysolar.org/, Accessed: 2021-12-01.

[48] pvlib website, https://pvlib-python.readthedocs.io, Accessed: 2021-12-01.

[49] J. Kerkmann, H. J. Lutz, M. König, Msg channels interpretation guide, https://rammb.cira.colostate.edu/wmovl/vrl/pptlectures/eumetsat/PowerPoints/Channels/conversion.ppt, Accessed: 2021-12-01 (2004).

[50] Y. University, Landsat 8: Greater than 1 reflectance values, https://surfaceheat.sites.yale.edu/sites/default/files/files/Greater%20than%201%20Reflectance%20Values.pdf, Accessed: 2021-12-01.

[51] EUMETSAT, Effective radiance and brightness temperature relation tables for meteosat second generation, https://www.eumetsat.int/media/37717, Accessed: 2021-12-01.

[52] GSICS, The conversion from effective radiances to equivalent brightness temperatures, https://www.eumetsat.int/media/8571, Accessed: 2021-12-01.

[53] GSICS, Another look at the seviri/iasi comparison in the 3.9 band, http://gsics.atmos.umd.edu/pub/Development/20210408/Coppens_IASI_for_3.9%C2%B5m_inter-calibration.pdf, Accessed: 2021-12-01.

[54] L. Benali, G. Notton, A. Fouilloy, C. Voyant, R. Dizene, Solar radiation forecasting using artificial neural network and random forest methods: Application to normal beam, horizontal diffuse and global components, Renewable Energy 132 (2019) 871–884. doi:https://doi.org/10.1016/j.renene.2018.08.044.
URL https://www.sciencedirect.com/science/article/pii/S0960148118309947

[55] Keras, Keras website, https://keras.io/, Accessed: 2021-12-01.

[56] Tensorflow, Tensorflow website, https://www.tensorflow.org/, Accessed: 2021-12-01.

[57] S. Ji, W. Xu, M. Yang, K. Yu, 3d convolutional neural networks for human action recognition, IEEE Transactions on Pattern Analysis and Machine Intelligence 35 (1) (2013) 221–231. doi:10.1109/TPAMI.2012.59.

[58] X. Shi, Z. Chen, H. Wang, D.-Y. Yeung, W.-k. Wong, W.-c. Woo, Convolutional lstm network: A machine learning approach for precipitation nowcasting (2015). doi:10.48550/ARXIV.1506.04214.
URL https://arxiv.org/abs/1506.04214

[59] D. P. Kingma, J. Ba, Adam: A method for stochastic optimization (2014). doi:10.48550/ARXIV.1412.6980.
URL https://arxiv.org/abs/1412.6980

[60] A. Kumler, Y. Xie, Y. Zhang, A new approach for short-term solar radiation forecasting using the estimation of cloud fraction and cloud albedo (10 2018). doi:10.2172/1476449.
URL https://www.osti.gov/biblio/1476449

[61] F. J. Rodríguez-Benítez, C. Arbizu-Barrena, J. Huertas-Tato, R. Aler-Mur, I. Galván-León, D. Pozo-Vázquez, A short-term solar radiation forecasting system for the iberian peninsula. part 1: Models description and performance assessment, Solar Energy 195 (2020) 396–412. doi:https://doi.org/10.1016/j.solener.2019.11.028.
URL https://www.sciencedirect.com/science/article/pii/S0038092X19311296

[62] G. S. Martins, M. Giesbrecht, Clearness index forecasting: A comparative study between a stochastic realization method and a machine learning algorithm, Renewable Energy 180 (2021) 787–805. doi:https://doi.org/10.1016/j.renene.2021.08.094.
URL https://www.sciencedirect.com/science/article/pii/S0960148121012623

[63] J. Nunes, Y. Bouaoune, E. Delechelle, O. Niang, P. Bunel, Image analysis by bidimensional empirical mode decomposition, Image and Vision Computing 21 (12) (2003) 1019–1026. doi:https://doi.org/10.1016/S0262-8856(03)00094-5.
URL https://www.sciencedirect.com/science/article/pii/S0262885603000945

[64] NASA, Landsat science, https://landsat.gsfc.nasa.gov/, Accessed: 2021-12-01.